Fluctuating initial conditions in heavy-ion collisions from the Glauber approach*

Wojciech Broniowski,[1,2,†] Piotr Bożek,[3,2,‡] and Maciej Rybczyński[1,§]

[1] *Institute of Physics, Świętokrzyska Academy, ul. Świętokrzyska 15, PL-25406 Kielce, Poland*
[2] *The H. Niewodniczański Institute of Nuclear Physics, PL-31342 Kraków, Poland*
[3] *Institute of Physics, Rzeszów University, PL-35959 Rzeszów, Poland*

(Dated: 28 June)

In the framework of the Glauber approach applied to the initial stage of ultra-relativistic heavy-ion collisions we analyze the shape parameters of the early-formed system (fireball) and their event-by-event fluctuations. We test a variety of models: the conventional wounded nucleon model, a model admixing binary collisions to the wounded nucleons, a model with *hot spots*, as well as the hot-spot model where the deposition of energy occurs with a superimposed probability distribution. We look in detail at the so-called *participant* harmonic moments, ε^*, obtained by an averaging procedure where in each event the system is translated to its center of mass and aligned with the major principal axis of the ellipse of inertia. Quantitative comparisons indicate substantial relative effects for ε^* in variants of Glauber models. On the other hand, the dependence of the scaled standard deviation $\Delta\varepsilon^*/\varepsilon^*$ on the chosen model is weak. For all models the values range from about 0.5 for the central collisions to about 0.3-0.4 for peripheral collisions, both for the gold-gold and copper-copper collisions. They are dominated by statistics and change only by 10-15% from model to model. We provide an approximate analytic expansion for the harmonic moments and their fluctuations given in terms of the fixed-axes moments. For central collisions and in the absence of correlations it gives the simple formula $\Delta\varepsilon^*/\varepsilon^* \simeq \sqrt{4/\pi - 1} = 0.52$. Similarly, we obtain expansions for the radial profiles of the higher harmonics. We investigate the relevance of the shape-fluctuation effects for jet quenching and find them important only for very central events. Finally, we make some comments of relevance for hydrodynamics, the elliptic flow and its fluctuations. We argue how smooth hydrodynamics leads to the known result $v_4 \sim v_2^2$, and further to the prediction $\Delta v_4/v_4 = 2\Delta v_2/v_2$.

PACS numbers: 25.75.-q, 25.75.Dw, 25.75.Ld
Keywords: relativistic heavy-ion collisions, Glauber model, wounded nucleons, event-by-event fluctuations, elliptic flow

arXiv:0706.4266v2 [nucl-th] 26 Aug 2007

I. INTRODUCTION

It was realized a few years ago in event-by-event hydrodynamic studies [1, 2] of relativistic heavy-ion collisions that fluctuations of the initial shape of the fireball formed in the early stage of the reaction lead to quantitatively important effects for azimuthal asymmetry [3, 4, 5, 6]. These effects, resulting from the shift of the center-of-mass and the rotation of the the quadrupole principal axis, can be seen in the analyses of the elliptic flow [7, 8, 9, 10]. The purpose of this paper is to investigate this phenomenon in detail in the framework of various Glauber-like approaches describing the deposition of energy in the system in the early stages of the collision. Our study focuses on both the understanding of the statistical nature of the results, as well as on comparisons of various models. The main outcome presented in this paper is twofold: first, we provide the Fourier moments and radial profiles of the so-called *participant* type, *i.e.* obtained with an averaging procedure where in each event the system is translated to its center of mass and aligned with the major principal axis. Second, under reasonable approximations we derive analytic expansions which explain the basic features of the Fourier moments and profiles.

The fact that the initial shape of the fireball fluctuates from event to event is certainly not surprising. Clearly, a finite number of sources consisting of wounded nucleons, binary collisions, *etc.*, which deposit the transverse energy in the system at mid-rapidity do not fill the available coordinate space uniformly due to statistical fluctuations. For instance, the center of mass of a system of uncorrelated particles fluctuates with a standard deviation proportional to $1/\sqrt{n}$. Similarly, the orientation of principal axis of the quadrupole and higher harmonic moments fluctuates from event to event. The statistical component of the harmonic moments assumes average values proportional $1/\sqrt{n}$, where n is the number of sources. Since the number of sources is not so large, ranging from a few to a few hundred, these fluctuations may easily reach a value of a few percent or higher, large for studies of azimuthal asymmetry where the investigated effects, such as the elliptic flow coefficient v_2, are of similar order. For the case of the wounded-nucleon model [11] and for the binary collisions the situation is illustrated in Fig. 1. The picture on the left shows all nucleons in both nuclei, the middle one the wounded nucleons, and the right one the binary collisions. We notice the mentioned effects for the distributions of the wounded nucleon and

*Supported by Polish Ministry of Science and Higher Education under grant N202 034 32/0918
†Electronic address: Wojciech.Broniowski@ifj.edu.pl
‡Electronic address: Piotr.Bozek@ifj.edu.pl
§Electronic address: Maciej.Rybczynski@pu.kielce.pl

the binary collisions: the twist of the principal axes, denoted by the skewed lines, and the displacement of the center of mass, represented by a dot at the intersection of the principal axes. Statistical analyses may be carried out in the reference frame fixed by the reaction plane (we call it *fixed-axes*), or (in each event) in the frame defined by the shifted and twisted principal axes of the quadrupole moment (we call it *variable-axes*[1]).

The first part of the paper discusses the fixed-axes and variable-axes harmonic moments and radial profiles obtained numerically from the Glauber Monte Carlo studies in several models: the conventional wounded-nucleon model [11], a model admixing binary collisions to wounded nucleons [12, 13], a model with *hot spots*, as well as the hot-spot model where the deposition of energy occurs with a given probability distribution (Sect. III). The results are presented in Sect. IV and V. The main result here is that the fixed-axes quadrupole moments, ε, and their scaled standard deviation, $\Delta\varepsilon/\varepsilon$, vary significantly from model to model. The same holds to a lesser extent for the variable-axes moments, ε^*. On the other hand, the dependence of the scaled standard deviation $\Delta\varepsilon^*/\varepsilon^*$ on the chosen Glauber-like model is weak, at most at the level of 10-15% for intermediate impact parameters. For all considered models the values range from about 0.5 for central collisions to about 0.3-0.4 for peripheral collisions. We examine the dependence on the mass number, providing results for the gold-gold and copper-copper collisions. We also investigate the effects of the assumed weighting power of the transverse radius in the definition of the harmonic moments, finding that the choice is not important for studies of fluctuations.

In Sect. VI we examine the role of the center-of-mass and quadrupole-axes fluctuations on jet quenching. Except for very central collisions, the effect of the increased eccentricity of the opaque medium is canceled by the shift of its position and axes rotation, leading to almost no change in the azimuthal asymmetry of the jets leaving the interaction region.

In Sect. VII we argue that the variable-axes quantities are dominated by sheer statistics and certain properties of variable-axes distributions can be explained in an elementary way through the use of the central limit theorem. In particular, in the absence of correlations between the location of sources and for central collisions we get the result of an appealing simplicity, namely $\Delta\varepsilon^*/\varepsilon^*(b=0) = \sqrt{4/\pi - 1} \simeq 0.52$, independent of the number of sources in the assumed model, the mass number of the colliding nuclei, or the collision energy. This result is fulfilled to a very good accuracy in actual numerical studies, where some correlations are present. For non-central collisions appropriate expansions are provided. We also analyze the variable-axes profiles in this way. The effects of correlations between the location of sources are discussed in Appendix D.

In Sect. VIII we propose another method of encoding the information on the initial state, where each harmonic (including the odd ones) is evaluated in its own eigenaxes. The method can be used as a base for a smoothing procedure in preparation of the initial conditions for event-by-event hydrodynamic studies.

In Sect. IX we make several comments referring to the collective flow. We note that the statistical analysis of the variable-axes parameters ε^* carries over to the analysis of the variable-axes elliptic-flow coefficient, v_2^*. For central collisions (in the absence of correlations) we find $\Delta v_2^*/v_2^*(b=0) = \sqrt{4/\pi - 1} \simeq 0.52$, independently of multiplicity, mass number, or the collision energy. This value is in the ball park of the recent experimental data [9, 10]. Moreover, under the assumption of smoothness that most likely holds in hydrodynamics, which allows for perturbation theory around the azimuthally symmetric solution, one obtains the relation $v_4^* \sim v_2^{*2}$ for the octupole flow coefficient. Consequently, for the event-by-event fluctuations we find the prediction $\Delta v_4^*/v_4^* = 2\Delta v_2^*/v_2^*$.

Appendices contain some more technical material, including the derivations of the statistical formulas. A simple one-dimensional toy model illustrating the essence of the statistical intricacies is given in Appendix C.

II. NOTATION

In our study we use the standard Woods-Saxon nuclear density profile for the nucleus of mass number A,

$$n(r) = \frac{c}{1+\exp(\frac{r-R}{a})}, \tag{2.1}$$

where the constant c, given in Appendix B, is such that the normalization $\int 4\pi r^2 dr\, n(r) = A$ is fulfilled. For the considered gold and copper nuclei the parameters are

$$R = 6.37 \text{ fm}, \quad a = 0.54 \text{ fm}, \quad (^{197}\text{Au}), \tag{2.2}$$
$$R = 4.14 \text{ fm}, \quad a = 0.57 \text{ fm}, \quad (^{62}\text{Cu}). \tag{2.3}$$

A popular way to simulate the short-range repulsion in Glauber-like calculations[2] is to enforce that the centers of nucleons in each nucleus cannot be closer to each other than the expulsion distance of $d = 0.4$ fm. This feature is simple to implement in Monte Carlo generators. Some details are provided in Appendix A.

We use the following standard convention for the axes of the reference frame: the z-axis is along the beam, the x-axis lies in the reaction plane, and the y-axis is

[1] We find this nomenclature more descriptive than the terms *standard* and *participant* used in the literature.

[2] We note that this repulsion increases slightly the size of the nucleus, but the effect is negligible, see Appendix A.

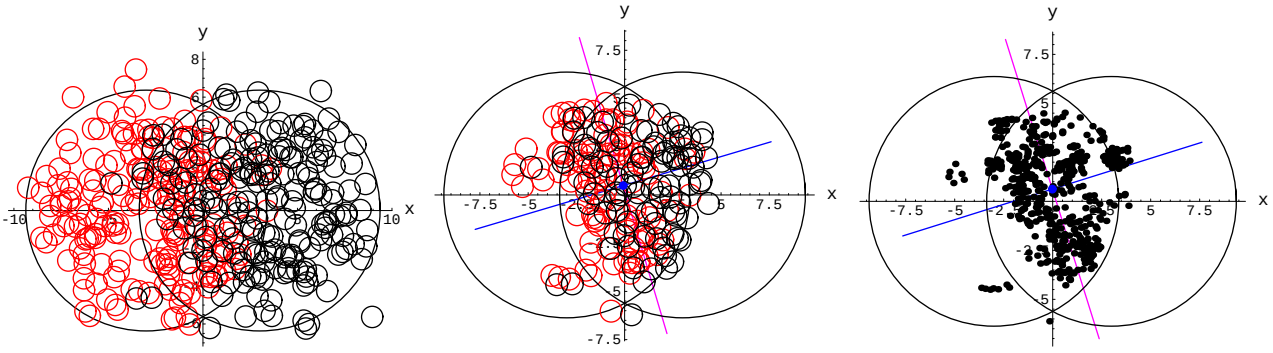


FIG. 1: (Color online) Snapshot of a typical gold-gold collision in the $x-y$ plane, $b=6$ fm. Red and black circles indicate nucleons from nuclei A and B, respectively, plotted with the size (3.2). The left picture shows all nucleons, the middle - the wounded nucleons only, and the right - the centers of mass of pairs of nucleons undergoing binary collisions. The straight lines indicate the (twisted) principal axis of the quadrupole moment, the blue dots show the center of mass of the system, while the outer circles denote the Woods-Saxon radius of gold, $R=6.37$ fm. The units on the x and y axes are fm.

perpendicular to the reaction plane. The azimuthal angle $\phi\in[-\pi,\pi]$ is measured relative to the y-axis, thus $y=\rho\cos\phi$, $x=\rho\sin\phi$, where ρ is the transverse radius.

We refer to the analysis in the fixed reference frame of the reaction plane as **fixed-axes** (sometimes called *standard* in the literature), and to the analysis where the particles in each event are translated to the center-of-mass frame and aligned with the major principal axis of the quadrupole moment as **variable-axes** (also called *participant*).

III. MODELS

We describe briefly the models studied in this paper. The standard implementation of the wounded nucleon model at RHIC energies assumes that the inelastic cross section of the nucleon is

$$\sigma_w = 42 \text{ mb}. \tag{3.1}$$

The nucleon from one nucleus gets wounded when it passes closer to a nucleon from the other nucleus than the hard-sphere radius

$$r_0=\frac{1}{2}\sqrt{\sigma_w/\pi}. \tag{3.2}$$

Then the weight $w=1/2$ is attributed to the point in the transverse plane at the position of the wounded nucleon. The weight can be thought of as a measure proportional to the amount of the deposition of the transverse energy, which then is carried away by the produced particles. For studies of fluctuations only the relative weights are important, and the overall normalization of the total weight can be chosen arbitrarily. In what follows we renormalize the distributions in all models to the number of the wounded nucleons, N_w.

For binary collisions the weight $w=1$ is attributed to each collision point, which is taken as the mean of the coordinates of the two colliding nuclei.

A successful description of multiplicities at RHIC has been achieved with a *mixed* model, amending the wounded nucleon model [11] with some binary collisions [12, 13]. In this case a wounded nucleon obtains the weight $w=(1-\alpha)/2$, and a binary collision the weight $w=\alpha$. The total weight averaged over events is then $(1-\alpha)N_{\rm w}/2+\alpha N_{\rm bin}$. The fits to particle multiplicities of Ref. [13] give $\alpha=0.145$ for collisions at $\sqrt{s_{NN}}=200$ GeV, and $\alpha=0.12$ for $\sqrt{s_{NN}}=19.6$ GeV.

Next, we consider a model with *hot spots* in the spirit of Ref. [14], assuming that the cross section for a semi-hard binary collisions producing a hot-spot is small, $\sigma_{\rm hot-spot}=0.5$ mb, but when such a rare collision occurs it produces on the average a large amount of transverse energy equal to $\alpha\sigma_{\rm w}/\sigma_{\rm hot-spot}$.

Each source from the previous models (wounded nucleon, mixed, or hot-spot) may deposit the transverse energy with a certain probability distribution. To incorporate this effect, we superimpose the Γ distribution over the distribution of sources, multiplying the weights of the considered model with the randomly distributed number from the gamma distribution

$$g(w,\kappa)=\frac{w^{\kappa-1}\kappa^{\kappa}\exp(-\kappa w)}{\Gamma(\kappa)}. \tag{3.3}$$

This distribution gives the average value equal to $\bar{w}=1$ and the variance $\text{var}(w)=1/\kappa$. This is at no loss of generality, since, as already mentioned, the individual weights used for carrying the statistical averages can be normalized arbitrarily. In this paper we do this superposition on the hot-spot model, where the considered effects are largest. Thus, we take the weights $(1-\alpha)g(w,\kappa)/2$ for the wounded nucleons and $\alpha g(w,\kappa)\sigma_{\rm w}/\sigma_{\rm hot-spot}$ for the binary collisions. We take $\kappa=0.5$, which gives $\text{var}(w)=5$. We label this model *hot-spot+*Γ.

The four considered models, **wounded nucleon**, **mixed**, **hot spot**, and **hot-spot+**Γ, differ by the number of sources and the amount of the built-in fluctuations.

For instance, the superposition of the Γ distribution with low values of k increases the variance. This increase is also generated with hot spots, which effectively reduce the number of sources. All these effects will be studied in detail below.

IV. FIXED-AXES HARMONIC MOMENTS

When the reaction plane is determined for each event (which of course can never be achieved exactly in the experiment, see *e.g.* Refs. [15, 16]), one can then choose the reference frame fixed by the reaction plane. The two-dimensional (boost-invariant) profile of the density of sources, $f(\rho,\phi)$, is obtained by averaging over the events belonging to a particular centrality or impact parameter class. The symmetry $f(\rho,\phi) = f(\rho,\pi-\phi)$ excludes odd components in the Fourier decomposition, while for equal colliding nuclei the symmetry $f(\rho,\phi) = f(\rho,-\phi)$ eliminates the $\sin(l\phi)$ functions. Thus,

$$f(\rho,\phi) = f_0(\rho) + 2f_2(\rho)\cos(2\phi) + 2f_4(\rho)\cos(4\phi) + \ldots, \tag{4.1}$$

where ρ is measured from the center of the geometric intersection of the two nuclei. The harmonic moments obtained form (4.1), which we call *fixed-axes*, are also called "standard" in the literature.

We first have a look at the Fourier profiles $f_l(\rho)$, where $l = 0, 2, 4, \ldots$. In Appendix B we show that at low values of ρ

$$f_l(\rho) \sim \rho^l, \quad (\rho \ll b), \tag{4.2}$$

while at high values of ρ

$$f_l(\rho) \sim \exp(-2\rho/a)\rho^2 \left(\frac{b}{\rho}\right)^l, \quad (\rho \gg b). \tag{4.3}$$

Such a behavior is typical of Fourier expansions of smooth functions.

We present the profiles $f_l(\rho)$ obtained with Monte Carlo simulations for the considered models in Fig. 2. The distributions in all models are normalized to the number of wounded nucleons, *i.e.*

$$\int \rho\, d\rho\, d\phi f(\rho,\phi) = \int 2\pi\rho d\rho f_0(\rho) = N_w. \tag{4.4}$$

We note that the profiles are substantially different from model to model. The monopole profile f_0 is broadest in the wounded nucleon model, then passing through the mixed model and the hot-spot model we arrive at the hot-spot+Γ model, which is most sharply peaked at the origin. Correspondingly, the quadrupole profiles $f_2(\rho)$ are concentrated further or closer to the origin. We note that the amplitude of subsequent harmonics decreases fast, such that taking l up to 4 is sufficient for any practical matter.

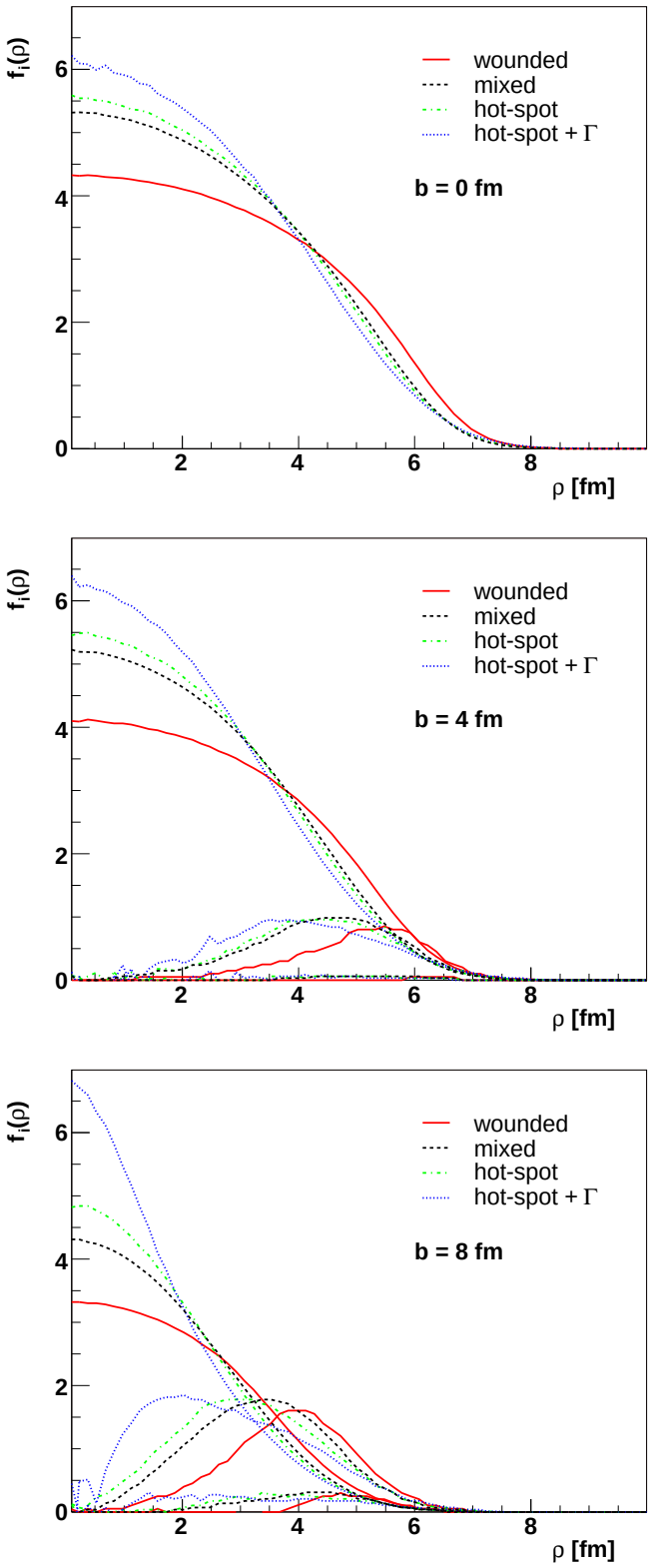


FIG. 2: (Color online) The *fixed-axes* profiles $f_i(\rho)$ for gold-gold collisions in the analyzed models at several values of the impact parameter: $b = 0, 4, 8$ fm. The legend explains the assignment of line-types to the models. For $b = 4$ and 8 fm for each model there are three curves, corresponding to $i = 0$, 2, and 4 from top to bottom. The $i = 4$ component is tiny.

In order to have some convenient quantitative measures of the profiles of Eq. (4.1) one introduces their radial moments

$$\varepsilon_{k,l} = \frac{\int 2\pi\rho f_l(\rho)\rho^k d\rho}{\int 2\pi\rho f_0(\rho)\rho^k d\rho} = \frac{I_{k,l}}{I_{k,0}}. \tag{4.5}$$

where we have introduced the moments

$$I_{k,l} = \frac{1}{N_w}\int_0^\infty 2\pi\rho d\rho f_l(\rho)\rho^k \tag{4.6}$$

for a future reference. The choice of the weighting power k is arbitrary, with the typical choice $k = 2$. Higher values of k make the measure more sensitive to the outer region of the system. We note that in the popular notation

$$\varepsilon_{\rm std} = \varepsilon_{2,2} \equiv \varepsilon. \tag{4.7}$$

We observe that in all the considered Glauber models ε is practically independent of the model (top panel of Fig. 3). Tiny differences come from different distributions of the wounded nucleons and binary collisions. On the other hand, the scaled standard deviation, shown at the lower panel of Fig. 3, displays a strong dependence on the model at low values of b, with the hot-spot+Γ model yielding about twice as much as the mixed model. We also notice a strong dependence on b. At $b = 0$ the curves diverge, which is an artefact of dividing by the vanishing value of ε. The fluctuations are larger in models effectively having the lower number of sources, which is obvious from the statistical point of view.

As already noted in Refs. [17, 18], the value of ε obtained with the color glass condensate (CGC) is substantially higher than in all Glauber-like models analyzed in this paper. For comparison, the CGC result is shown as the upper curve in the top panel of Fig. 3. After the e-print version of this paper has been posted, a calculation of fluctuations of ε^* in the CGC framework has appeared [19]. The results are overlayed in in the bottom part Fig. 7. We note that at intermediate values of b the CGC values of $\Delta\varepsilon^*/\varepsilon^*$ are significantly lower than in the considered Glauber models.

In Fig. 4 we show the results for the octupole moment, $\varepsilon_{4,2}$, and its standard deviation, obtained in the wounded-nucleon model. We note a very flat shape of $\varepsilon_{4,2} \sim b^4$ at low b. This behavior is a direct consequence of integrating Eqs. (4.2,4.3). The standard deviation grows with increasing impact parameter. In other models considered in this paper the results are qualitatively similar.

V. VARIABLE-AXES HARMONIC MOMENTS

As is well known, the reaction plane cannot be determined precisely in an experiment, or not at all, which originated multiple methods of analyzing azimuthal asymmetry in heavy-ion collisions. As has recently been realized [1, 2, 3, 4, 5, 6], the purely statistical

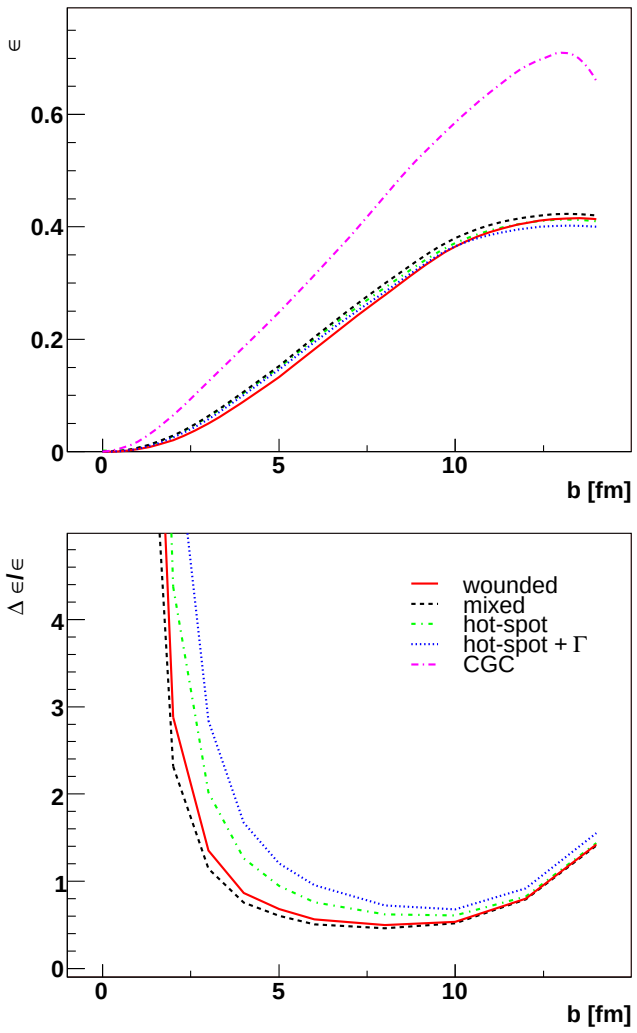


FIG. 3: (Color online) The harmonic moment $\varepsilon \equiv \varepsilon_{2,2}$ and its scaled standard deviation for the analyzed models plotted as functions of the impact parameter. The result for the color-glass condensate comes from Ref. [17]. Gold-gold collisions.

fluctuations caused by the finite number of particles lead to sizeable effects of the *variable geometry* in the initial stage of the collision. The effect can be seen qualitatively in Fig. 1, where we notice a highly irregular shape of the distributions of both the wounded nucleons and the binary-collisions distribution. The mere presence of the fluctuation of the initial condition is obvious. What is somewhat surprising, however, is its size, leading to noticeable effects in the analysis of azimuthal asymmetry even at large numbers of participating nucleons.

The center of mass of the distribution of the sources is not located at the geometrical center of the overlap of the two-colliding nuclei. In each event it is shifted in the x and y directions by Δx and Δy, defined as

$$\Delta x = \frac{\sum_i x_i w_i}{\sum_i w_i}, \quad \Delta y = \frac{\sum_i y_i w_i}{\sum_i w_i},. \tag{5.1}$$

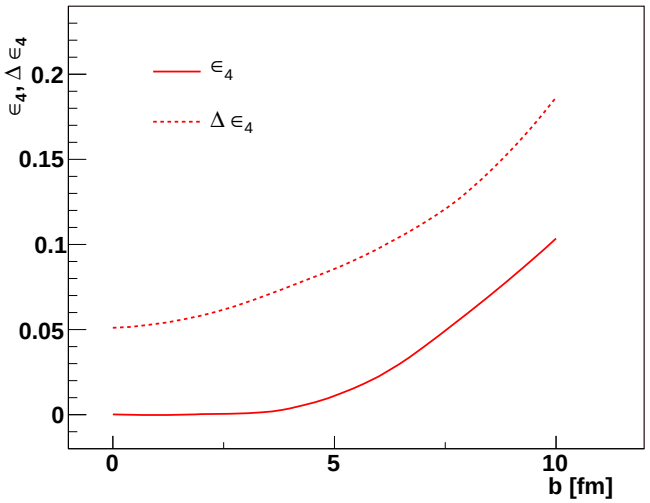


FIG. 4: (Color online) The fixed-axes octupole moment, $\varepsilon_4 \equiv \varepsilon_{2,4}$, and its standard deviation, plotted as functions of the impact parameter. Wounded nucleon model, gold-gold collisions.

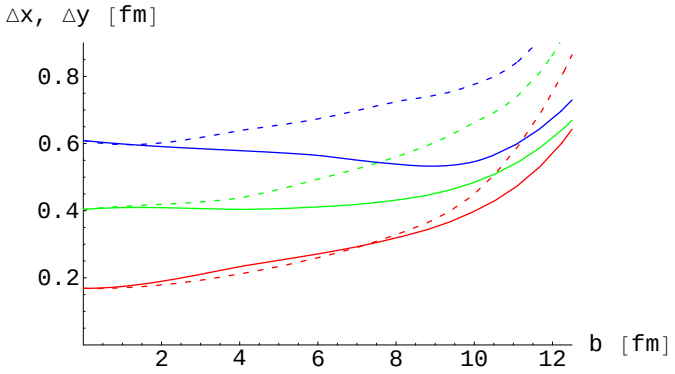


FIG. 5: (Color online) The root mean square shifts of the center of mass in the in-plane direction, Δx (solid lines), and in the out-of-plane direction, Δy (dashed lines). The lower lines are for the wounded-nucleon, the middle for the hot-spot, and the upper for the hot-spot+Γ model.

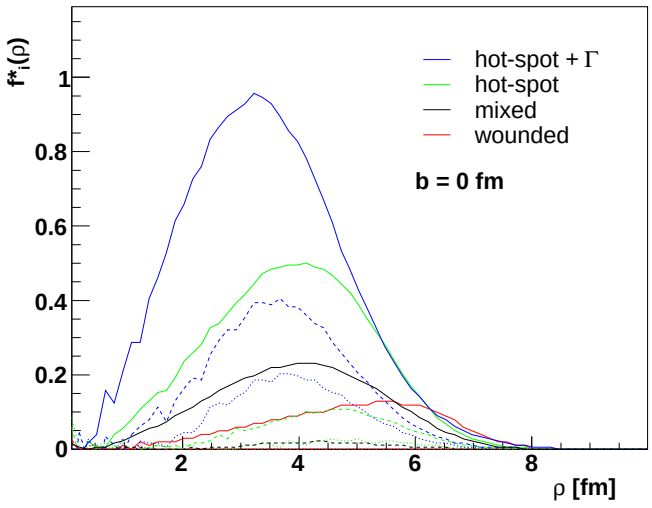
where i labels the sources and w_i denotes the weights. For an uncorrelated distribution of a large number of sources n one has

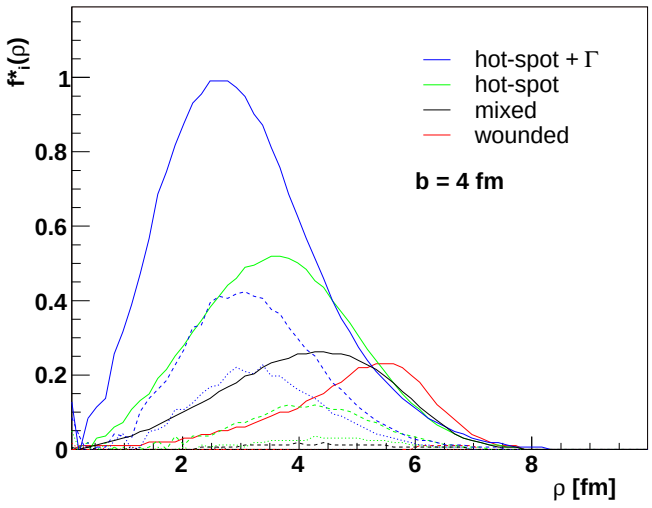
$$(\Delta x)^2 = \frac{1}{n} R_x^2 \langle w^2 \rangle, \quad (\Delta y)^2 = \frac{1}{n} R_y^2 \langle w^2 \rangle, \tag{5.2}$$

where

$$R_x^2 = \frac{1}{N_w} \int f(\rho,\phi) \rho^3 \sin^2\phi d\rho d\phi,$$
$$R_y^2 = \frac{1}{N_w} \int f(\rho,\phi) \rho^3 \cos^2\phi d\rho d\phi, \tag{5.3}$$

are the mean squared radii of the geometric fixed-axes distribution, and $\langle w^2 \rangle = \int dw\, w^2 g(w,\kappa)$. Since our system exhibits some correlation between the location of





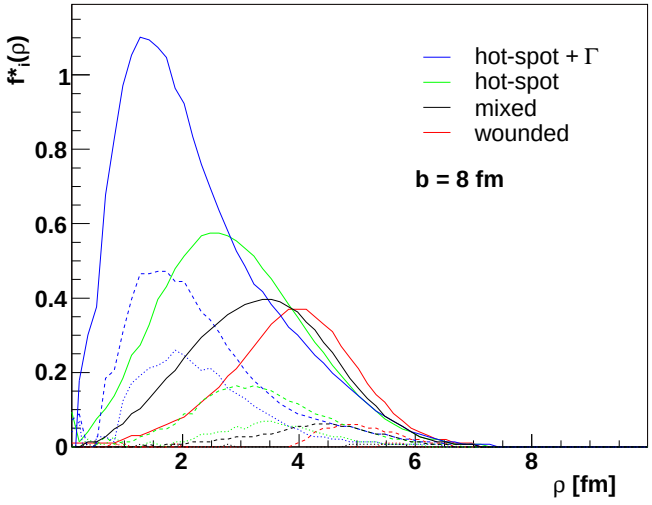


FIG. 6: (Color online) The *variable-axes* profiles $f_i^*(\rho)$ for the analyzed models at several values of the impact parameter. The solid, dashed, and dotted lines correspond to $i = 2$, 4, and 6, respectively. The four models: hot-spot+Γ, hot-spot, mixed, and the wounded nucleon model yield curves arranged from the top to bottom, respectively. Gold-gold collisions.

sources, the formula (5.2) is not realized exactly, but hold qualitatively. In Fig 5 we show Δx and Δy as functions of the impact parameter for the wounded-nucleon (lower curves), the hot-spot (middle curves) and the hot-spot+Γ (top curves) models. The shift is more important for peripheral collisions, where n is lower, even though the source size itself decreases.

The shift of the center of mass is physically relevant in the jet analysis, because it moves apart the formed fireball from the jet production points (Sect. VI).

In each event one can compute the principal axes of the ellipse of inertia. This corresponds to the choice $k = 2$ as the weighting power. The angle between the major half-axis of the ellipse and the y axis is given by

$$\tan(2\phi^*) = 2\frac{\langle xy\rangle - \langle x\rangle\langle y\rangle}{\mathrm{var}(y) - \mathrm{var}(x)}, \tag{5.4}$$

where the brackets denote the averaging over the particles within the given event. Importantly, in the variable-axes calculations all coordinates in the given event are always shifted by $(\Delta x, \Delta y)$ such that $\langle x\rangle = \langle y\rangle = 0$.

The angle ϕ^* fluctuates sizably from event to event. In our notation, the superscript $*$ indicates quantities averaged in such a way, that first in each event the rotation angle ϕ^* is determined according to Eq. (5.4), then the rotation is performed to the current principal-axis system, and finally the summation is done. As a result,

$$\begin{aligned} f^*(\rho,\phi) &= f_0^*(\rho) + 2f_2^*(\rho)\cos(2\phi - 2\phi^*) \\ &+ 2f_4^*(\rho)\cos(4\phi - 4\phi^*) + \dots \end{aligned} \tag{5.5}$$

We call the above profiles the *variable-axes* profiles. Obviously, $f_0^*(\rho) = f_0(\rho)$ and $f_l^*(\rho) \geq f_l(\rho)$ for each ρ.

In analogy to Eq. (4.5) we introduce the variable-axes moments

$$\varepsilon_{k,l}^* = \frac{\int 2\pi\rho f_l^*(\rho)\rho^k}{\int 2\pi\rho f_0^*(\rho)\rho^k}, \tag{5.6}$$

In the common notation for the variable-axes or participant deformation parameter one has

$$\varepsilon_{\mathrm{part}} = \varepsilon_{2,2}^* \equiv \varepsilon^*. \tag{5.7}$$

The profiles and moments for higher harmonics are suppressed, similarly to the fixed-axes case. This is clear, as the higher harmonics are evaluated relative to the axes determined by maximizing the quadrupole moment. As a result, only a few moments are needed to effectively parameterize the profile.

Figure 6 shows the variable-axes profiles for $l = 2, 4, 6$ (the $l = 0$ profiles are equal to the fixed-axes case) for all considered models. The line-types distinguish the Fourier label l, while the hot-spot+Γ, hot-spot, mixed, and the wounded nucleon models yield curves for each l arranged from the top to bottom, respectively. Comparing Figs. 2 and 6 we note sizeable departures of the variable-axes profiles f_l^* from the fixed-axes profiles f_l ($l = 2, 4, \dots$), in particular at small values of the impact parameter. For

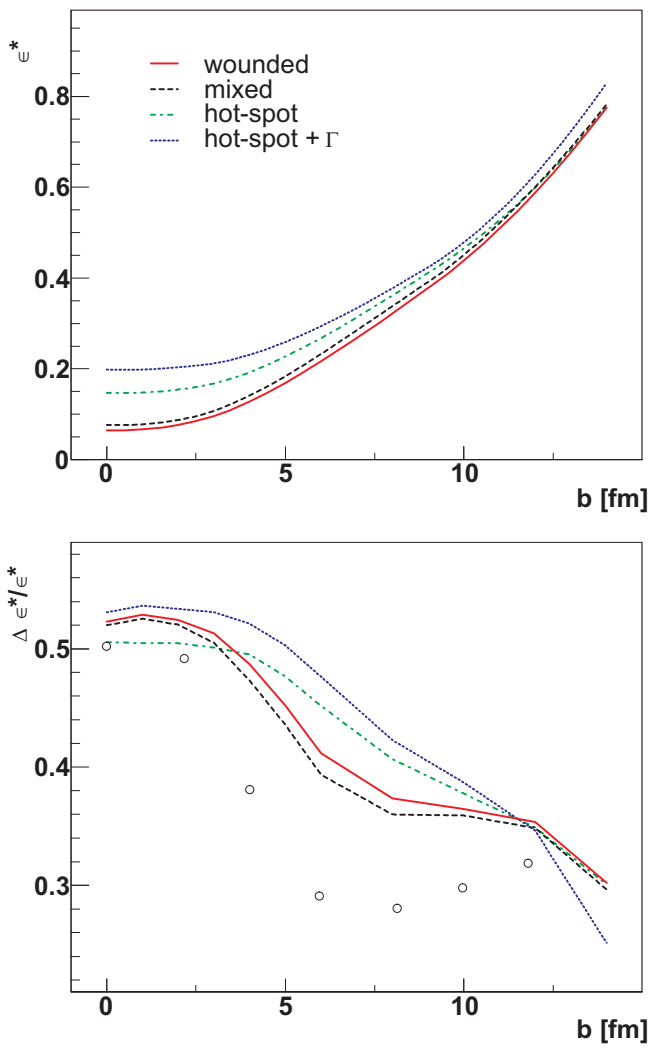


FIG. 7: (Color online) The harmonic moment $\varepsilon^* \equiv \varepsilon_{2,2}^*$ and its scaled standard deviation for the analyzed models plotted as functions of the impact parameter. Gold-gold collisions. The open circles in the bottom figure show the calculation in the color-glass-condensate framework taken from Ref. [19].

the central collisions ($b = 0$) the variable-axes profiles are non-zero solely due to fluctuations, as will be discussed in Sect. VII.

In Fig. 7 we show the quadrupole moment ε^* and its scaled standard deviation. We observe a strong model dependence of ε^* at low values of b, with models having effectively lower number of sources yielding higher values. At $b = 0$ the hot-spot+Γ model yields three times more than the wounded nucleon model. For all models the scaled standard deviation is close to the value 0.5 for central collisions and drops to about 0.3 at $b = 14$ fm. We argue in Sect. VII why the central value is always close to 0.5, independently of the effective number of sources. At intermediate values of b the relative difference in $\Delta\varepsilon^*/\varepsilon^*$ between various considered models is at the level of 10-15%, which is not a very strong effect.

TABLE I: Dependence of the quadrupole asymmetry parameters on the weighting power k from definitions (4.5,5.6)

k	0	2	4	6
$b = 0$				
$\varepsilon^*_{k,2}$	0.047	0.064	0.089	0.121
$\Delta\varepsilon^*_{k,2}/\varepsilon^*_{k,2}$	0.53	0.52	0.52	0.52
$b = 8$ fm				
$\varepsilon_{k,2}$	0.147	0.278	0.388	0.466
$\Delta\varepsilon_{k,2}/\varepsilon_{k,2}$	0.44	0.48	0.48	0.49
$\varepsilon^*_{k,2}$	0.176	0.319	0.452	0.555
$\Delta\varepsilon^*_{k,2}/\varepsilon^*_{k,2}$	0.44	0.38	0.34	0.31

We have examined numerically the role of the weighting power of the radius, k, entering the definitions (4.5,5.6). This is important for the method, since as pointed out earlier, the value of k is arbitrary. The result is that both $\varepsilon_{k,2}$ and $\varepsilon^*_{k,2}$ increase substantially with k, however the scaled standard deviation remains quite stable, in particular at low impact parameters. The results are collected in Table I. We vary k between 0 and 6, which is a wide range. At $b = 0$ the scaled standard deviation remains practically constant, while at $b = 8$ it varies by 10% for the fixed-axes case and 25% for the variable-axes case. Due to this rather weak dependence, the particular choice of the weighting power k is not essential in studies of this quantity in event-by-event fluctuations. However, the values of ε and ε^* itself are sensitive to the choice of k. As already mentioned, the higher values of k increase the sensitivity to the profiles at higher values of the transverse radius ρ.

In Fig. 8 we present the variable-axes harmonic moments and their scaled standard deviation for the copper-copper collisions. Due to the much lower number of sources compared to the gold-gold case of Fig. 7, we note higher values of ε^* at low b. On the other hand, the scaled standard deviation is remarkably similar to the gold-gold case, especially at low b, as should be according to the arguments of Sect. VII. Certainly, the dependence on the mass number is a sensitive probe of the whole approach.

In Sect. VII we will show that many of the qualitative and quantitative features of the Fourier distributions as well as their moments have simple explanations on purely statistical grounds.

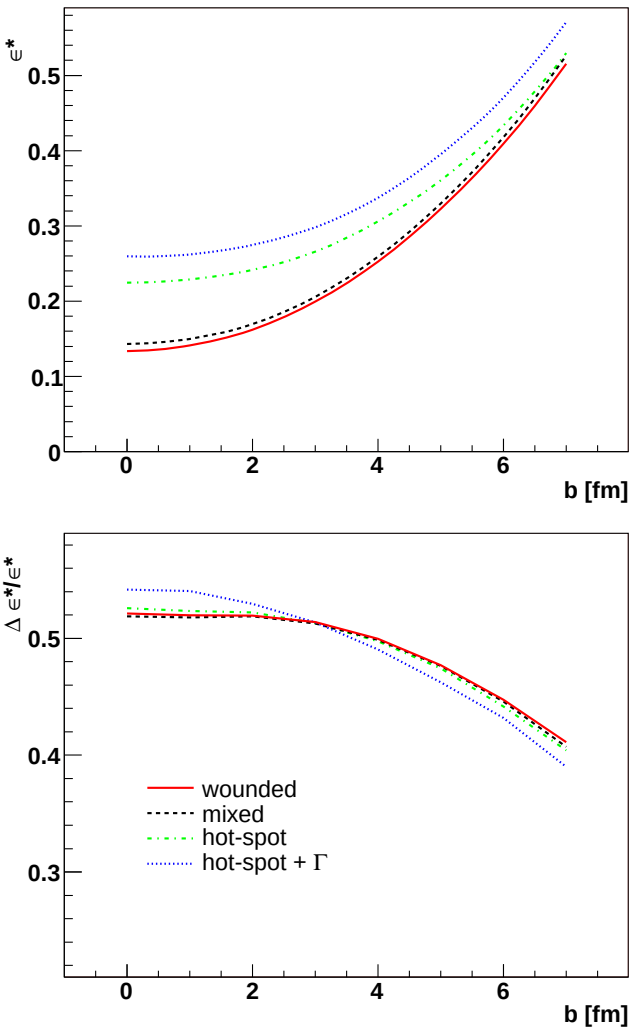


FIG. 8: (Color online) Same as Fig. 7 for the copper-copper collisions.

VI. JET QUENCHING

Jet quenching in dense matter occurs mainly at the very first stages of the collision [20, 21]. The values of the nuclear modification factor

$$R_{AA}(p_T) = \frac{\frac{dN_{AA}}{d^2p_T}}{N_{\rm coll}\frac{dN_{pp}}{d^2p_T}}$$

measured in central Au+Au collisions for $p_T > 3$ GeV fall significantly below 1. The dependence of the nuclear modification factor on centrality can be understood as due to the change of the size of the opaque medium which modifies the mean length of the path of the jet in the fireball. On the other hand the azimuthal asymmetry of the high-p_T particles is believed to be a consequence of the geometric eccentricity of the medium. The difference of the path lengths for the jets moving "in plane" and "out of plane" leads to an asymmetry in the jet energy loss [22, 23, 24]. The angle-averaged nuclear modification factor R_{AA} is very weakly dependent on the shape of the opaque medium, once its size has been fixed.

In this paper we use a simple model [24, 25] of the energy loss in order to explore the role of the shape of the event-by-event rotated absorbing medium. Neglecting the transverse expansion of the fireball for early times relevant for jet quenching, we expect that the shape of the medium is close to the initial conditions as obtained from the distribution of sources in the transverse plane from the Glauber models. Several prescriptions for the

distribution of the density in the transverse plane have been used, such as the wounded nucleon density, the binary collisions density, the mixed density, or the color glass condensate estimate. All of these approaches use an event-averaged shape of the medium in which the jets propagate. However, it is clear that in each particular event the thermalized dense medium has a slightly different shape and position with respect to the geometric reaction plane. In order to take this into account, one can use the variable-axes density $f^*(\rho,\phi)$ as the density of the scattering centers for the propagating parton. The resulting increase of the eccentricity of the medium is expected to increase the asymmetry of the jet absorption. A very similar effect has been discussed for source the profiles calculated including saturation in the CGC model. Drescher et al. [26] have found an increase in v_2 by about $10-15\%$.

The partons are produced in p-p collisions with the power-law spectrum $dN/dp_T^2 \propto 1/p_T^{8.1}$ (the fragmentation is not included), and the energy loss is taken as

$$\Delta E = \mu E \int_0^\infty l dl \frac{\tau_0}{l+\tau_0} f^*(x_0+v_x(l+\tau_0), y_0+v_y(l+\tau_0)), \tag{6.1}$$

where the jet production point $(x_0,\ y_0)$ is generated from a binary collision in the fixed-axes frame. The fact that we must use the fixed-axes frame here results from an absence of correlations of the very rare jet-production collisions and the soft collisions generating the opaque medium. In Eq. (6.1) the initial time is denoted as τ_0, while the time measured from τ_0 is l. The direction of the parton transverse velocity $(v_x,\ v_y)$ is chosen randomly. For each choice of the model of the opaque medium the parameter μ in the energy loss formula (6.1) is fitted to reproduce the high-p_T nuclear modification factor R_{AA} [27]. Then the elliptic flow coefficient is calculated at different centralities (v_2 and R_{AA} are p_T-independent in such a simplified model). The variable-axes medium has a different shape from the fixed-axes one, with a larger eccentricity. As has been noticed, the raise in the geometrical eccentricity increases the asymmetry of the energy loss [26]. The variable-axes medium in the hot-spot model has an eccentricity of about 0.4, and the CGC calculation gives 0.5 at intermediate impact parameters, therefore one would expect a similar increase in v_2 at high p_T. However, there is one important effect that should be taken into account for the event-by-event modified absorbing medium. The absorbing medium formed in each event is rotated and also shifted. The shift with respect to the fixed-axes frame is quite important (*cf.* Fig. 5), yielding about 1/3 of the total effect.

The resulting elliptic flow (Fig. 9) at centralities larger than 20% resulting from the energy loss calculated with the wounded-nucleon model in the fixed-axes frame (solid line) comes out remarkably similar to the result of the hot-spot model in the variable-axes frame (dashed line). Only when the shift and rotation of the opaque medium are neglected (dotted line) the modification of the shape leads to an increase of the high p_T elliptic flow coefficient

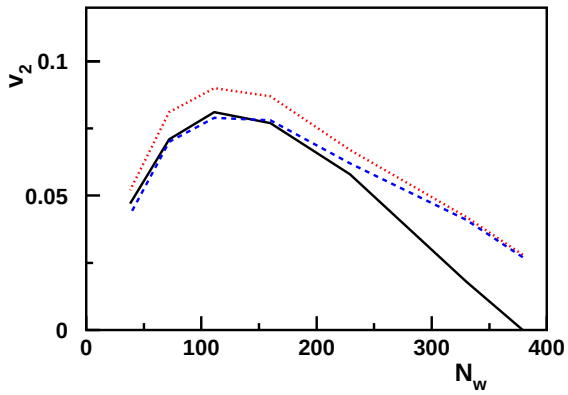


FIG. 9: (Color online) Elliptic flow coefficient at high p_T as a function of the number of wounded nucleons, obtained using the fixed-axes density of the wounded nucleons $f(x,y)$ in the energy loss formula 6.1 (solid line), and with the variable-axes density $f^*(x,y)$ for the hot-spot scenario (dashed line). The dotted line represents the result for the variable-axes density but without the shift and rotation of the opaque medium.

v_2 by about $10-15\%$, We have checked that the cancellation of the effects of the increased eccentricity of the medium and of the shift and rotation with respect to the jet emission points at larger centralities happens also for other considered models.

In the forthcoming experiments at the Large Hadron Collider (LHC) the analysis of jet tomography with respect the the event-by-event reconstructed plane must take into account the relative shift and rotation effects discussed above.

VII. STATISTICAL INTERPRETATION OF THE VARIABLE-AXES MOMENTS

In this section we analyze the variable-axes moments and profiles from the viewpoint of statistical methods. The purpose of this study is to understand certain features of the numerical results presented earlier on more general formal grounds. It turns out that quite simple expressions can be found for the case where correlations between the location of sources are neglected, which allows for the standard usage of the central limit theorem. The Glauber models do induce some correlations, as can be seen from Fig. 1. For instance, a nucleon from the skin of one of the nuclei, as present in the middle picture, wounds several nucleons from the other nucleus. As a result, correlation between the locations of the wounded nucleons is generated. For simplicity, we neglect all such correlations in the analytic analysis of this section. Their role is discussed in Appendix D.

If such correlations are strong, their analytic inclusion is difficult and one has to resort to numerical simulations such as those presented in the earlier sections. We also take all weights equal to unity, $w_i = 1$, in order to avoid notational complications.

Appendix C contains a very simple analysis in a one-dimensional independent-particle toy model, which avoids some notational complications but grasps all essential features of the full case.

From definition of the variable-axes moment, we need to evaluate

$$\begin{aligned}\varepsilon^*_{k,l} &= \langle\langle \frac{\frac{1}{n}\sum_{j=1}^n \rho_j^k \cos[l(\phi_j-\phi^*)]}{\frac{1}{n}\sum_{j=1}^n \rho_j^k}\rangle\rangle \\ &= \frac{1}{I_{k,0}}\langle\langle \frac{1}{n}\sum_{j=1}^n \rho_j^k \cos[l(\phi_j-\phi^*)]\rangle\rangle, \end{aligned} \quad (7.1)$$

with $\langle\langle . \rangle\rangle$ denoting the averaging over (infinitely many) events and j labeling the source. The weighting, according to the definition (4.5), is done with the transverse radius to the power k, *i.e.* ρ_j^k. Let us introduce the notation

$$Y_l = \frac{1}{n}\sum_{j=1}^n \rho_j^k \cos(l\phi_j), \quad X_l = \frac{1}{n}\sum_{j=1}^n \rho_j^k \sin(l\phi_j) \quad (7.2)$$

(recall that we measure the azimuthal angle from the y-axis). The rotation angle ϕ^* depends on the distribution of particles in the given event, by definition maximizing the *quadrupole* moment ($l=2$), *i.e.* the quantity $\frac{1}{n}\sum_{j=1}^n \rho_j^k \cos[2(\phi_j-\phi^*)]$. This gives the relations

$$\begin{aligned}\cos(2\phi^*) &= Y_2/\sqrt{Y_2^2+X_2^2}, \\ \sin(2\phi^*) &= X_2/\sqrt{Y_2^2+X_2^2}, \end{aligned} \quad (7.3)$$

Let us denote $x_j = (\rho_j, \phi_j)$ as the short-hand notation for the polar coordinates of the source point, and $F(x_1, x_2, \ldots, x_n)$ as the n-particle probability distribution. Then we can rewrite Eq. (7.1) as

$$\begin{aligned}&\varepsilon^*_{k,l} = \frac{1}{I_{k,0}}\int dx_1 \ldots dx_n F(x_1,\ldots,x_n) \times \quad (7.4)\\ &\frac{1}{n}\sum_{j=1}^n \rho_j^k [\cos(l\phi_j)\cos(2\phi^*) - \sin(l\phi_j)\sin(2\phi^*)] = \\ &\frac{1}{I_{k,0}}\int dx_1 \ldots dx_n F(x_1,\ldots,x_n)\frac{Y_l Y_2 + X_l X_2}{\sqrt{Y_2^2+X_2^2}}. \end{aligned}$$

Let us analyze the quadrupole moment $\varepsilon^*_{k,2}$, which is the simplest but also the most important measure. For that case Eq. (7.1) becomes

$$\begin{aligned}&\varepsilon^*_{k,2} = \frac{1}{I_{k,0}}\int dx_1 \ldots dx_n F(x_1,\ldots,x_n)\sqrt{Y_2^2+X_2^2} = \\ &\frac{1}{I_{k,0}}\langle\langle\sqrt{Y_2^2+X_2^2}\rangle\rangle = \quad (7.5)\\ &\frac{1}{nI_{k,0}}\langle\langle\sqrt{\left(\sum_{j=1}^n \rho_j^k\cos(2\phi_j)\right)^2 + \left(\sum_{j=1}^n \rho_j^k \sin(2\phi_j)\right)^2}\rangle\rangle. \end{aligned}$$

Thus, the variable-axes quadrupole moment corresponds to a highly "non-local" average, involving infinitely many moments through the square root function.

In the absence of correlations between collision points the many-particle probability distribution factorizes into $F(x_1,\ldots,x_n) = f(x_1)\ldots f(x_n)$, where $f(x_i)$ are normalized to unity. Hence all the information on the system is contained in the one-particle distribution functions (4.1), or, equivalently, in the *fixed-axes* profiles $f_l(\rho)$. The variable-axes profiles $f^*_l(\rho)$ and moments $\varepsilon^*_{k,l}$ are then expressible in terms of the fixed-axes quantities. In order to get some useful relations, we use a method similar to the techniques of Refs. [15, 28, 29]. In the limit of large n the goal is accomplished with the help of the central limit theorem. Indeed, the variables $\rho^k\cos(2\phi)$ and $\rho^k\sin(2\phi)$ entering Eq. (7.5) are independent from one another, since $\int_0^{2\pi}\rho^{2k}\cos(2\phi)\sin(2\phi)=0$. Therefore for sufficiently large values of n one may use the central limit theorem, implying the normal distribution for the variables Y_2 and X_2. The details of this calculation are given in Appendix D. The final results can be cast in the form of a series involving the confluent hypergeometric functions:

$$\begin{aligned}&\varepsilon^*_{k,2} = \frac{\sqrt{2}\sigma^2_{Y_2}}{I_{k,0}\sqrt{\pi}\sigma_{X_2}}\sum_{m=0}^{\infty}(2\delta\sigma^2_{Y_2})^m \times \quad (7.6)\\ &\frac{\Gamma\left(m+\frac{1}{2}\right)\Gamma\left(m+\frac{3}{2}\right)\ {}_1F_1\left(-\frac{1}{2};m+1;-\frac{\bar{Y}_2^2}{2\sigma^2_{Y_2}}\right)}{m!^2}, \end{aligned}$$

where the average and standard deviation of the variables (7.2) are (see Appendix D)

$$\begin{aligned}\bar{Y}_2 &= I_{k,2}, \quad (7.7)\\ \sigma^2_{Y_2} &= \frac{1}{2n}(I_{2k,0} - 2I^2_{k,2} + I_{2k,4}) \\ \sigma^2_{X_2} &= \frac{1}{2n}(I_{2k,0} - I_{2k,4}), \\ \delta &= \frac{1}{2\sigma^2_{Y_2}} - \frac{1}{2\sigma^2_{X_2}}. \end{aligned}$$

For the special case of central collisions (where $\delta=0$) only the $m=0$ piece contributes to the series (7.6) and we have the very simple result

$$\varepsilon^*_{k,l} = \frac{\sqrt{\pi I_{2k,0}}}{2I_{k,0}\sqrt{n}}, \qquad (b=0). \quad (7.8)$$

Similarly, for the scaled standard deviation in central collisions we obtain (see Appendix D)

$$\frac{\Delta\varepsilon^*_{k,l}}{\varepsilon^*_{k,l}} = \sqrt{\frac{4}{\pi}-1} \simeq 0.523, \qquad (b=0) \quad (7.9)$$

Although the above result is approximate, as it has been obtained with the assumption of no two-particle correlations between the location of sources, it shows an important feature present in the Glauber simulations. The

value of the scaled standard deviation in central collisions is close to 0.5 and is asymptotically independent of n (*cf.* Figs. 7 and 8). The behavior is also seen in the numbers given in Table I for $b = 0$.

One may also derive the expression for the profile function $f_2^*(\rho)$ in the large-n limit and for the case with no correlations. For central collisions the result is (see Appendix D)

$$f_2^*(\rho) \simeq \frac{1}{2}\sqrt{\frac{\pi}{nI_{2k,0}}}\,\rho^k f_0(\rho), \qquad (b=0) \qquad (7.10)$$

Thus the variable-axes quadrupole profile is proportional to the monopole profile times ρ^k. Note that this behavior reflects the chosen weighting power k, hence in this sense is technical rather than physical. One verifies that Eq. (7.10) reproduces immediately Eq. (7.8).

VIII. MULTIPLE-AXES PROFILES

In Eq. (5.5) the rotation angle ϕ^* has been fixed with the quadrupole moment. All higher harmonics were obtained with respect to this angle. One can give another prescription, which is superior for encoding the shape of the system for studies of event-by-event fluctuations. For a distribution of sources in each event we may provide the harmonic profile, as well as its orientation relative to the y axis. Thus, each profile f_l^* has its own rotation angle ϕ_l^*. We introduce the expansion (the meaning of $*$ is now different than in Sect. V and IX)

$$f^*(\rho,\phi) = f_0^*(\rho) + 2f_2^*(\rho)\cos(2\phi - 2\phi_2^*) \qquad (8.1)$$
$$+2f_3^*(\rho)\cos(3\phi - 3\phi_3^*) + 2f_4^*(\rho)\cos(4\phi - 4\phi_4^*) + \ldots$$

This expansion is complete, as

$$\begin{aligned}\cos(l\phi - l\phi_l^*) &= \cos(l\phi)\cos(l\phi_l^*) + \sin(l\phi)\sin(l\phi_l^*) = \\ &= a_l\cos(l\phi) + b_l\sin(l\phi), \qquad (8.2)\end{aligned}$$

which provides the full Fourier expansion of the distribution in each event, including both the sine and cosine functions. Note also the presence of odd moments, $l = 3, 5, \ldots$. These moments average out to zero in the limit of infinitely many events, but have non-zero fluctuations from event to event.

In Fig. 10 we show the *multiple-axes* profiles for the wounded nucleon model for the first few harmonics. We note that there is no longer a strong suppression as l is increased. Clearly, to describe completely the full shape of the distribution we need as many harmonics as sources! In actual applications certain smoothing must be included, which effectively cuts off the higher harmonics from the expansion. These equilibration processes cause sharp shapes to smooth out, *i.e.* high harmonics are damped. One may therefore propose a smoothing prescription based on multiple-axes profiles, introducing a suitable cut-off function in the Fourier index l. Details

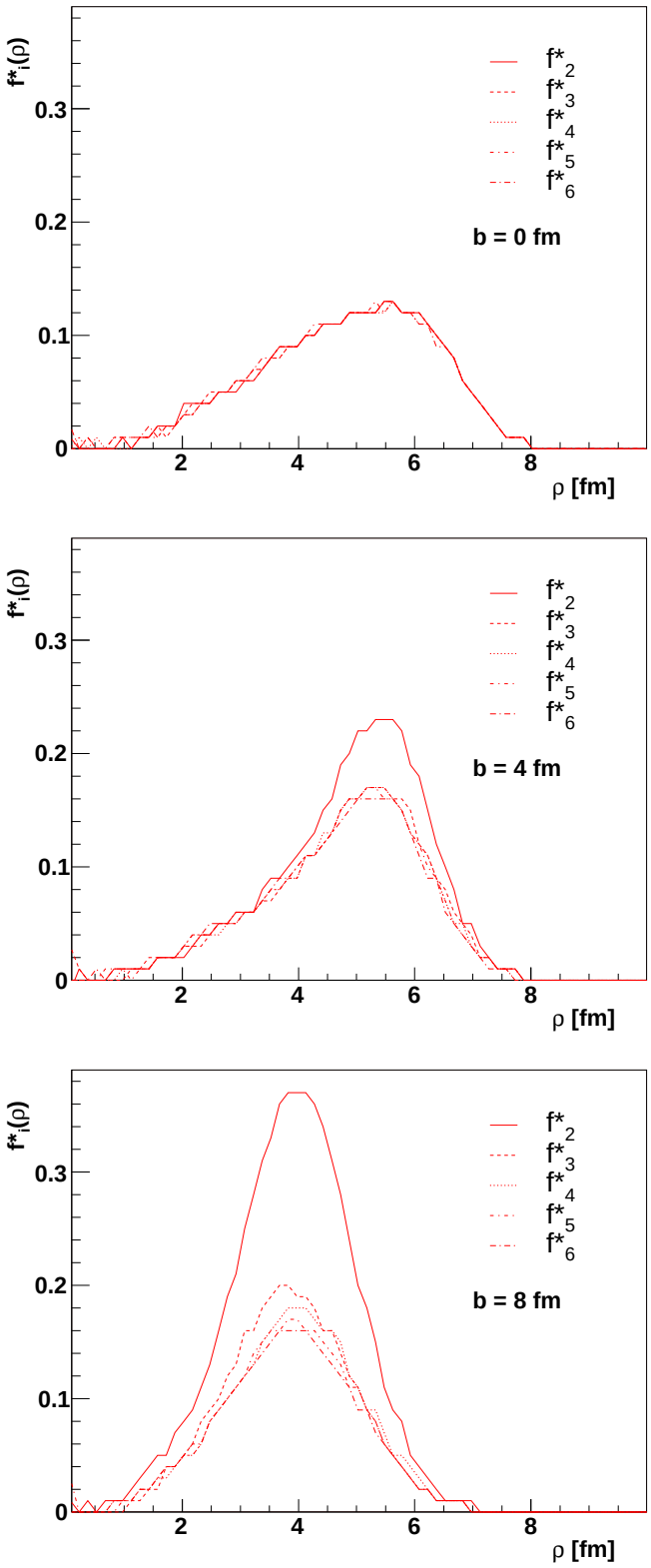


FIG. 10: (Color online) The *multiple-axes* profiles $f_i^*(\rho)$, $i = 2, 3, 4, 5, 6$, for the wounded nucleon model at several values of the impact parameter b. Gold-gold collisions.

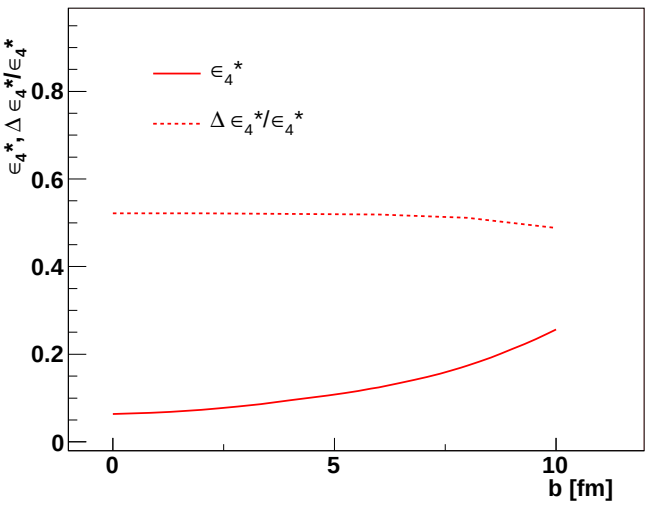


FIG. 11: (Color online) The multiple-axes octupole moment, $\varepsilon_4^* \equiv \varepsilon_{2,4}^*$, and its scaled standard deviation, plotted as functions of the impact parameter. Wounded nucleon model, gold-gold collisions.

and application to event-by-event hydrodynamics will be presented elsewhere.

In Fig. 11 we show the results for the multiple-axes octupole moment, $\varepsilon_{4,2}^*$, and its scaled standard deviation for the case of gold-gold collisions. As explained above, this moment is computed in each event in the reference frame which maximizes the octupole distribution. We note that again at $b = 0$ the scaled standard deviation is close to 0.5, as in the large-n limit and in the absence of correlations it assumes the value $\Delta\varepsilon_{l,k}^*/\varepsilon_{l,k}^*(b=0) = \sqrt{4/\pi - 1}$. The details of the analysis are given in Appendix D.

IX. FLUCTUATIONS OF THE ELLIPTIC FLOW

The statistical analysis for the fluctuations of the variable-axes shape parameters, in particular ε^*, carries over to the fluctuations of the elliptic flow coefficient v_2^*. These fluctuations, which are an important probe of the nature of the early-stage dynamics of the system [30], have recently been measured at RHIC [8, 9, 10]. In fact, the experimental procedure used in these analyses identifies the elliptic flow coefficient with the *participant* or variable axes v_2, here denoted as v_2^*.

The relevance of studies of fluctuations of the initial shape of the fireball comes from the well-known fact that for small elliptic asymmetry one expects on hydrodynamic grounds the relation

$$\frac{\Delta v_2^*}{v_2^*} = \frac{\Delta\varepsilon^*}{\varepsilon^*}. \tag{9.1}$$

As argued in Ref. [31], the result (9.1) indicates that the mean free path in the matter created in the initial stages of the heavy-ion collisions is very small, although turbulence does not develop.

The statistical method used in Sect. V carries over to v_2^*. An immediate consequence of Eq. (9.1), under the assumption of the absence of correlations between the location of sources, is the result for the variable-axes coefficient, v_2^*, in central collisions:

$$\frac{\Delta v_2^*}{v_2^*}(b=0) \simeq \sqrt{\frac{4}{\pi} - 1} \simeq 0.52. \tag{9.2}$$

The values obtained in Refs. [9, 10] for the scaled standard deviation of v_2^* are between 0.35 and 0.5 for all impact parameters.

An argumentation for the result (9.1) may be done on general grounds as follows: schematically, one may denote the hydrodynamic equations as $L(\psi) = 0$, where L is the operator for hydrodynamics (involving partial differentiation, *etc.*), and ψ is the set of hydrodynamic functions of space-time describing the state of the system. If the evolution is *smooth*, one may expand to first order around the azimuthally-symmetric system ψ_0,

$$L(\psi) = L(\psi_0 + \delta\psi) \simeq L(\psi_0) + L'(\psi_0)\delta\psi, \tag{9.3}$$

where $\delta\psi$ is the asymmetric piece, and the prime denotes the differentiation with respect to the hydrodynamic variables ψ. Since $L(\psi_0) = 0$, we have to first order $L'(\psi_0)\delta\psi = 0$. Then, due to linearity of the equation for $\delta\psi$, we have $||\delta\psi(t)|| \sim ||\delta\psi(t_0)||$, *i.e.*, the magnitude of the solution at time t is proportional to the initial condition at t_0. This concerns all hydrodynamic properties, in particular the shape and flow. As a result, the v_2^* coefficient determined from the momentum spectra at time t is proportional to the initial spatial quadrupole asymmetry ε^*. The feature holds event-by-event, hence the result (9.1) follows. Thus Eq. (9.1) is a consequence of applicability of perturbation theory for the small departure from cylindrical symmetry.

We note that Eq. (9.1) holds separately for the fixed-axes and the variable-axes analyses, with the obvious requirement to use the same method on both sides of the equation.

One may ask if a similar argumentation can be used for the higher harmonic flow coefficients, v_4^*, *etc.* The results of the previous sections show a strong suppression of subsequent harmonic moments of the distribution of sources in the case of the fixed-axes and variable-axes analyses. This suggests the hierarchy

$$\psi = \psi_0 + \lambda\delta\psi_2 + \lambda^2\delta\psi_4 + \ldots, \tag{9.4}$$

where λ, typically of the order of a few percent, is the small expansion parameter, while the subscripts $0, 2, 4, \ldots$ label the harmonics. Expansion of the hydrodynamic evolution to second order in λ, again under the assumption of smoothness, yields now

$$\begin{aligned} L(\psi) &= L(\psi_0) + \lambda L'(\psi_0)\delta\psi_2 \\ &+ \lambda^2\left[L'(\psi_0)\delta\psi_4 + L''(\psi_0)(\delta\psi_2)^2/2\right] + \ldots \end{aligned} \tag{9.5}$$

We carry out the perturbation theory extracting the second-order equation,

$$L'(\psi_0)\delta\psi_4 = -L''(\psi_0)(\delta\psi_2)^2/2, \tag{9.6}$$

and note that the evolution of $\delta\psi_4$ is coupled to $(\delta\psi_2)^2$, which acts as a source term in the linear inhomogeneous equation for $\delta\psi_4$.

Various harmonic components evolve hydrodynamically with different time scales. Let us denote τ_2 as the characteristic time for the operator $L'(\psi_0)$, or $\delta\psi_2$, and τ_4 as the characteristic time for the operator $L''(\psi_0)$. If

$$\tau_2 \gg \tau_4, \tag{9.7}$$

then the time scale for the source term in Eq. (9.6) is much larger than for the operator $L''(\psi_0)$. In that case for $t \gg t_0$

$$||\psi_4(t)|| \sim ||\delta\psi_2(t)||^2 \sim ||\delta\psi_2(t_0)||^2. \tag{9.8}$$

In words, at late times the octupole deformation is proportional to the square of the initial quadrupole deformation, and looses memory of the initial octupole deformation $||\psi_4(t_0)||$. In particular, this means that

$$v_4^* \sim \varepsilon^{*2} \sim v_2^{*2}. \tag{9.9}$$

In Ref. [32] the variable v_4/v_2^2 has been suggested as a sensitive probe of the hydrodynamic evolution. Also, the simulations of Refs. [32, 33] show that with increasing time the value of v_2 saturates (suggesting very large τ_2), while v_4 quickly assumes the value proportional to v_2^2, supporting the assumption $\tau_2 \gg \tau_4$ used in the above argumentation. The data of Refs. [34] comply to the result (9.9), perhaps except for very low values of the transverse momenta.

For the fluctuations one gets immediately from Eq. (9.9)

$$\frac{\Delta v_4^*}{v_4^*} = 2\frac{\Delta v_2^*}{v_2^*} = 2\frac{\Delta\varepsilon^*}{\varepsilon^*}. \tag{9.10}$$

Relation (9.10), if verified experimentally, would support the scenario of smooth hydrodynamic evolution with the mentioned hierarchy of scales.

At sufficiently late times *all* deformations are determined by the initial ε^*. This results in other relations, for instance for the azimuthal Hanbury-Brown–Twiss (HBT) correlation radius, $R_{\rm HBT}(\phi)$, one expects

$$R_4 \sim R_2^2, \tag{9.11}$$

where $R_{\rm HBT}(\phi) = R_0 + 2R_2\cos(2\phi) + 2R_4\cos(4\phi) + \ldots$

X. CONCLUSION

We have presented a comprehensive study of the shape fluctuations in a variety of Glauber-like models. Here is the list of our main points:

1. We compare four Glauber-like models, with different degree of fluctuation: the wounded-nucleon model, the mixed model, the hot-spot model, and the hot-spot model with the superimposed Γ distribution.

2. We obtain numerically the fixed-axes and variable-axes harmonic profiles and analyze their moments. The variable-axes moments ε^*, and the fixed-axes scaled standard deviation $\Delta\varepsilon/\varepsilon$ are sensitive to the choice of the variant of the Glauber model, while the $\Delta\varepsilon^*/\varepsilon^*$ is not, changing at most by 10-15%. At intermediate values of b the results of the Glauber-like models for $\Delta\varepsilon^*/\varepsilon^*$ lie significantly above the color-glass-condensate predictions of Ref. [19].

3. We present expansions for the variable-axes moments and profiles. These analytic formulas explain the features of the simulations, in particular, they show that at $b = 0$ the multiple-axes scaled variances are close to the value 0.5, insensitive of the model used, the mass number of the colliding nuclei, or the collision energy. In essence, the behavior of the scaled variance, used as a popular measure of the event-by-event fluctuations, is governed by the statistics.

4. Unlike the results of Ref. [26] which finds an increase of the jet elliptic flow v_2 at the level of 10%, we find that the effect of the increased quadrupole eccentricity is largely canceled by the shift of the center of mass and rotation of the axes of the absorbing medium. This leads to practically no change of the jet emission asymmetry at intermediate and large impact parameters. Only for small impact parameters the appearance of the quadrupole moment in the shape of the medium wins over the relatively less important shift and rotation.

5. We propose to use an improved harmonic expansion, the multiple-axes expansion, where the harmonics in each event are evaluated with their own reference frame. Such a scheme may be a starting point for the event-by-event hydrodynamic studies. The details will be presented elsewhere.

6. The analysis of the variable-axes moments in the coordinate space directly carries over to the collective flow and analysis of v_2^* in the momentum space. In particular, Eq. (9.2) holds for the variable-axes elliptic flow coefficient.

7. Finally, we comment that under plausible assumptions of smoothness, the hydrodynamic evolution leads to sensitivity of higher flow harmonics, v_4, *etc.* to the initial *quadrupole* deformation only. Higher harmonics of the deformation are irrelevant. Then Eq. (9.9) or (9.10) follow.

Acknowledgments

MR is grateful to Zbigniew Włodarczyk for fruitful discussions. WB thanks Paul Sorensen, Constantin Loizides, and Wit Busza for helpful discussions concerning the experimental determination of v_2 and its fluctuations.

APPENDIX A: DETAILS OF THE MONTE-CARLO PROCEDURE

The 3-dimensional positions of the nucleons in a nucleus are randomly generated from the Woods-Saxon distribution (2.1). Whenever the center of a nucleon is generated closer than the expulsion distance of $d = 0.4$ fm to a center of any of the prior generated nucleons, this nucleon is discarded and generated anew. The procedure results in a certain "swelling" phenomenon. However, for the chosen value of $d = 0.4$ fm the effect is tiny, increasing the R parameter by 0.01 fm only, which is a small fraction of a percent. The swelling effect could be compensated by reducing appropriately the original R parameter of the distribution (2.1). At higher values of the expulsion distance d the swelling effect increases. For instance, if one chose $d = 1$ fm, then the resulting size parameter is $R = 6.575$ fm, 3% larger than needed, and then the compensation in the original value of R should be done.

APPENDIX B: PROPERTIES OF THE FIXED-AXES HARMONIC PROFILES

At fixed values of b the shape of the profiles $f_l(\rho)$ reflects in a simple manner the average distribution of sources in a given model. Let us assume that $d = 0$, *i.e.* we ignore the short-range correlations, which complicate the analysis. The nucleus thickness function is

$$T(s) = \int_{-\infty}^{\infty} dz n\left(\sqrt{s^2+z^2}\right), \tag{B1}$$

with the density function n defined in Eq. (2.1). The normalization is $\int 2\pi s ds T(s) = A$. In the wounded nucleon model one has the following formula for the density of sources in the collision of large nuclei A an B:

$$\begin{aligned} n_W(\boldsymbol{b},\boldsymbol{\rho}) &= T_A(\boldsymbol{\rho}+\boldsymbol{b}/2)\left[1-\exp(-\sigma_w T_B(\boldsymbol{\rho}-\boldsymbol{b}/2))\right] \\ &+ T_B(\boldsymbol{\rho}-\boldsymbol{b}/2)\left[1-\exp(-\sigma_w T_A(\boldsymbol{\rho}+\boldsymbol{b}/2))\right]. \end{aligned} \tag{B2}$$

The corresponding formula for the binary collisions is

$$N_{\rm bin}(\boldsymbol{b},\boldsymbol{\rho}) = \sigma_{\rm bin} T_A(\boldsymbol{\rho}+\boldsymbol{b}/2) T_B(\boldsymbol{\rho}-\boldsymbol{b}/2). \tag{B3}$$

Let us introduce the short-hand notation $u = \rho^2 + b^2/4$, $v = \rho b \sin\phi$. We may then rewrite Eq. (B2,B3) in a more explicit form

$$\begin{aligned} N_w(u,v) &= T_A(u+v)\left[1-\exp(-\sigma_w T_B(u-v))\right] \\ &+ T_B(u-v)\left[1-\exp(-\sigma_w T_A(u+v))\right], \\ N_{\rm bin}(u,v) &= \sigma_{\rm bin} T_A(u+v) T_B(u-v). \end{aligned} \tag{B4}$$

When $\rho \ll b$ then $v \ll u$ and the low-ρ expansion of the source density corresponding to Eqs. (B4) has the form $\sum_n c_n \rho^{2n} \sin^{2n}\phi$. Because $\int_0^{2\pi} d\phi \sin^{2n}\phi \cos(2m\phi)$, needed for the the decomposition (4.1), vanishes at $n > m$, we obtain the result (4.2).

The normalization constant in the Woods-Saxon function (2.1) is

$$c = -A/\left[8\pi a^3 {\rm Li}_3\left(-e^{R/a}\right)\right]. \tag{B5}$$

Here ${\rm Li}_n(z) = \sum_{k=1}^{\infty} z^k/k^n$ denotes the polylogarithm function. At high values of ρ the function (2.1) asymptotes to $c\exp\left((R-r)/a\right)$. Correspondingly, the nucleus thickness function at large s becomes

$$T(s) \sim c\sqrt{2\pi a s}\, e^{-s/a}. \tag{B6}$$

For $\rho \gg b$ we also have $v \ll u$, hence with a calculation similar as for low ρ we find Eq. (4.3).

APPENDIX C: THE TOY PROBLEM

This Appendix contains a detailed description of a toy model illustrating in a simple manner the statistical techniques used in the full-fledged calculation. Consider the one-dimensional problem (in the azimuthal angle ϕ) where we randomly generate uncorrelated particles from a distribution containing the monopole and quadrupole moments only,

$$f(\phi) = 1 + 2\epsilon\cos(2\phi), \quad \epsilon \in [-\frac{1}{2}, \frac{1}{2}]. \tag{C1}$$

The distribution has two fixed-axes moments,

$$\begin{aligned} f_0 &= \frac{1}{2\pi}\int_0^{2\pi} d\phi f(\phi) = 1, \\ f_2 &= \frac{1}{2\pi}\int_0^{2\pi} d\phi \cos(2\phi) f(\phi) = \epsilon. \end{aligned} \tag{C2}$$

Suppose we generate randomly n particles according to the distribution (C1) in each event, and subsequently carry the averaging of the results over the events, denoted as $\langle\langle . \rangle\rangle$. For instance, f_2 is estimated as

$$f_2 \simeq \langle\langle \frac{1}{n}\sum_{k=1}^{n} \cos(2\phi_k)\rangle\rangle, \tag{C3}$$

where k labels the particles in each event. The equality becomes strict as the number of events approaches infinity, which we assume implicitly from now on.

For the variable-axes quadrupole moment we need to rotate the particles with the rotation angle ϕ^*, which changes from event to event. Thus we need to evaluate (f_2^* has the meaning of ε^* from the other parts of the paper)

$$f_2^* = \langle\langle \frac{1}{n}\sum_{k=1}^{n} \cos[2(\phi_k - \phi^*)]\rangle\rangle. \tag{C4}$$

The rotation angle ϕ^* depends itself on the distribution of particles in the given event. It is such that the quantity $A = \frac{1}{n}\sum_{k=1}^{n}\cos[2(\phi_k - \phi^*)]$ assumes maximum, which gives the conditions $dA/d\phi^* = 0$, $d^2A/d(\phi^*)^2 < 0$. The solution is

$$\begin{aligned} \cos(2\phi^*) &= Y_2/\sqrt{Y_2^2 + X_2^2}, \\ \sin(2\phi^*) &= X_2/\sqrt{Y_2^2 + X_2^2}, \end{aligned} \tag{C5}$$

where we have introduced the short-hand notation

$$Y_2 = \frac{1}{n}\sum_{k=1}^{n}\cos(2\phi_k), \quad X_2 = \frac{1}{n}\sum_{k=1}^{n}\sin(2\phi_k). \tag{C6}$$

Using the above formulas in Eq. (C4) yields

$$\begin{aligned} f_2^* &= \langle\langle\sqrt{Y_2^2 + X_2^2}\rangle\rangle \\ &= \langle\langle\sqrt{\left(\frac{1}{n}\sum_{k=1}^{n}\cos(2\phi_k)\right)^2 + \left(\frac{1}{n}\sum_{k=1}^{n}\sin(2\phi_k)\right)^2}\,\rangle\rangle. \end{aligned} \tag{C7}$$

We see that the variable-axes moment corresponds to an average of the square root of sums (C5), thus is a highly "non-local" object.

For sufficiently large multiplicity of the events, n, one may evaluate Eq. (C7) with the help of the central limit theorem. Consider the variables $c_k = \cos(2\phi_k)$ and $s_k = \sin(2\phi_k)$. The average is

$$\bar{c} = \langle\langle\frac{1}{n}\sum_{k=1}^{n} c_k\rangle\rangle = \frac{1}{2\pi}\int_0^{2\pi} d\phi\cos(2\phi)f(\phi) = \epsilon, \tag{C8}$$

while for the variance we have

$$\begin{aligned} \sigma_c^2 &= \langle\langle\frac{1}{n}\sum_{k=1}^{n} c_k^2\rangle\rangle - \bar{c}^2 \\ &= \frac{1}{2\pi}\int_0^{2\pi} d\phi\cos(2\phi)^2 f(\phi) - \epsilon^2 = \frac{1}{2} - \epsilon^2. \end{aligned} \tag{C9}$$

Likewise, for the s_k variable

$$\begin{aligned} \bar{s} &= \langle\langle\frac{1}{n}\sum_{k=1}^{n} s_k\rangle\rangle = \frac{1}{2\pi}\int_0^{2\pi} d\phi\sin(2\phi)f(\phi) = 0, \\ \sigma_s^2 &= \langle\langle\frac{1}{n}\sum_{k=1}^{n} s_k^2\rangle\rangle = \frac{1}{2}. \end{aligned} \tag{C10}$$

Importantly, there is no correlation between Y_2 and X_2, as

$$\langle\langle\frac{1}{n}\sum_{k=1}^{n} c_k s_k\rangle\rangle = \frac{1}{2\pi}\int_0^{2\phi} d\phi\cos(2\phi)\sin(2\phi)f(\phi) = 0. \tag{C11}$$

According to the central limit theorem, the distribution of the Y_2 and X_2 variables is Gaussian,

$$\begin{aligned} f(Y_2, X_2) &= \frac{n}{2\pi\sigma_c\sigma_s}\exp\left[-n\left(\frac{(Y_2 - \bar{c})^2}{2\sigma_c^2} + \frac{X_2^2}{2\sigma_s^2}\right)\right] \\ &= \frac{n}{\pi\sqrt{1-2\epsilon^2}}\exp\left[-n\left(\frac{(Y_2 - \epsilon)^2}{1-2\epsilon^2} + X_2^2\right)\right]. \end{aligned} \tag{C12}$$

Introducing the notation

$$\begin{aligned} Y_2 &= q\cos\alpha, \quad X_2 = q\sin\alpha, \quad q^2 = Y_2^2 + X_2^2, \\ \delta &= \frac{1}{2\sigma_c^2} - \frac{1}{2\sigma_s^2} = \frac{1}{1-2\epsilon^2} - 1, \end{aligned} \tag{C13}$$

we may write

$$\begin{aligned} f(q,\alpha) &= \frac{n}{\pi\sqrt{1-2\epsilon^2}} \times \\ &\exp\left[-n\left(\frac{q^2 + \epsilon^2 - 2q\epsilon\cos\alpha}{1-2\epsilon^2}\right) + n\delta q^2\sin^2\alpha\right]. \end{aligned} \tag{C14}$$

What we will need below is the integral of this distribution over α,

$$\begin{aligned} \int_0^{2\pi} d\alpha f(q,\alpha) &= \frac{2n}{\sqrt{\pi}\sqrt{1-2\epsilon^2}}\exp\left[-n\left(\frac{q^2+\epsilon^2}{1-2\epsilon^2}\right)\right] \\ &\times\sum_{j=0}^{\infty}(2q\epsilon)^j\,\frac{\Gamma(j+\frac{1}{2})}{j!}I_j\left(\frac{2n\epsilon q}{1-2\epsilon^2}\right). \end{aligned} \tag{C15}$$

As a check, it follows that

$$\begin{aligned} &\int q\,dq\,d\alpha\,f(q,\alpha) \\ &= \frac{\sqrt{1-2\epsilon^2}}{\sqrt{\pi}}\sum_{j=0}^{\infty}\left(2\epsilon^2\right)^j\frac{\Gamma(j+\frac{1}{2})}{j!} = 1, \end{aligned} \tag{C16}$$

where we have use the definitions (C13) and the formula

$$\sum_{j=0}^{\infty} A^j\frac{\Gamma(j+\frac{1}{2})}{j!} = \sqrt{\frac{\pi}{1-A}}. \tag{C17}$$

We may now evaluate the variable-axes moment (C4). We have the following series:

$$\begin{aligned} f_2^* &= \int q\,dq\,d\alpha\,q f(q,\alpha) = \frac{1-2\epsilon^2}{\sqrt{n\pi}}\sum_{j=0}^{\infty}\left(2\epsilon^2\right)^j \\ &\times\ \frac{\Gamma(j+\frac{1}{2})\Gamma(j+\frac{3}{2})}{j!^2}{}_1F_1\left(-\frac{1}{2}, j+1; -\frac{n\epsilon^2}{1-2\epsilon^2}\right). \end{aligned} \tag{C18}$$

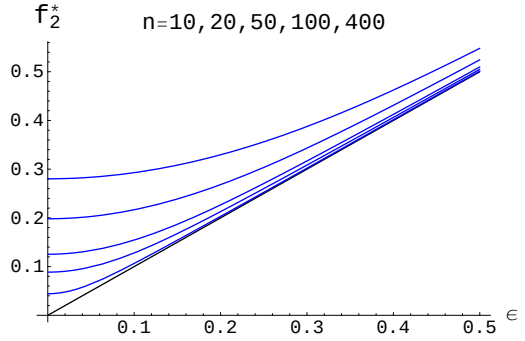


FIG. 12: (Color online) Toy model. Dependence of the variable-axes moment f_2^* on the fixed-axes quadrupole moment ϵ for several values of the number of particles n. As n increases, we pass from to to bottom with the presented curves. The straight line is the $n \to \infty$ limit, *i.e.* $f_2^* = \epsilon$. We note that the effect of the departure of f_2^* from ϵ is strongest at low ϵ and low n.

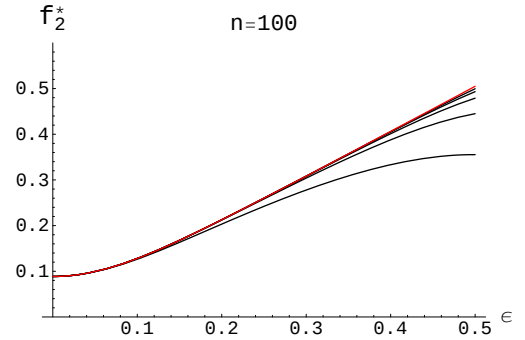


FIG. 13: (Color online) Toy model. The rate of convergence of the series (C18). The curves from bottom to top we show, correspondingly, the results of summing up 1, 2, 3, 4, and 5 terms, as well as the full result.

We were not able to sum up this series into a closed form, but one may readily use it for practical calculations in a truncated form. At $\epsilon = 0$ we have

$$f_2^*(\epsilon = 0) \;=\; \frac{\sqrt{\pi}}{2\sqrt{n}}, \tag{C19}$$

which shows the expected $1/\sqrt{n}$ behavior for a statistical fluctuation.

The numerical results of the series (C18) are presented in Fig. 12. We note that the effect of the departure of f_2^* from ϵ is strongest at low ϵ and low n.

Figure 13 shows the rate of convergence of the series (C18) for $n = 100$, where we show the subsequent results of summing up 1, 2, 3, 4, and 5 terms. We note that 5 terms are sufficient to achieve accuracy better than 1%.

We note that an expansion of the result in powers of ϵ is useless due to slow convergence properties. The first few terms are

$$f_2^* \;=\; \frac{\sqrt{\pi}}{2\sqrt{n}}\left(1 + \frac{n-1}{2}\epsilon^2 - \frac{n^2-6n+3}{16}\epsilon^4 + \mathcal{O}\left(n^3\epsilon^6\right)\right), \tag{C20}$$

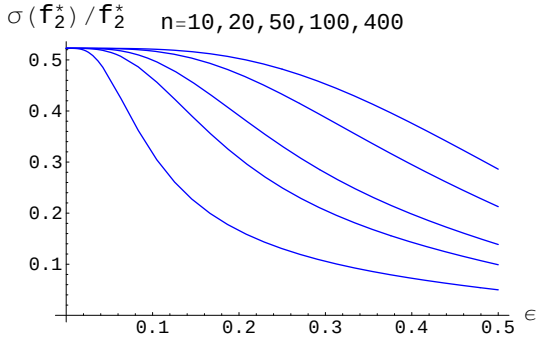


FIG. 14: (Color online) Toy model. The dependence of the scaled standard deviation on ϵ for several values of the number of particles n. The curves from top to bottom correspond to $n = 10$, 20, 50, 100, and 400, respectively.

hence the effective expansion parameter is $n\epsilon^2$. Thus for large values of n the convergence radius in ϵ is very small.

The evaluation of the second moment in the q variable yields

$$\langle\langle Y_2^2 + X_2^2\rangle\rangle = \int q\,dq\,d\alpha\,q^2 f(q,\alpha) = \frac{\sqrt{1-2\epsilon^2}}{n\sqrt{\pi}} \times \sum_{j=0}^{\infty} \frac{\left(2\epsilon^2\right)^j \left((-2j+n-2)\epsilon^2 + j + 1\right)\Gamma\left(j+\frac{1}{2}\right)}{j!} = \frac{1+(n-1)\epsilon^2}{n}. \tag{C21}$$

The obtained result is obvious from a direct evaluation form the definition. We compute

$$\langle\langle Y_2^2 + X_2^2\rangle\rangle = \tag{C22}$$
$$\langle\langle \left(\frac{1}{n}\sum_{k=1}^{n}\cos(2\phi_k)\right)^2 + \left(\frac{1}{n}\sum_{k=1}^{n}\sin(2\phi_k)\right)^2 \rangle\rangle =$$
$$\langle\langle \frac{1}{n} + \frac{1}{n^2}\sum_{k\neq j}\left(\cos(2\phi_j)\cos(2\phi_k) + \sin(2\phi_j)\sin(2\phi_k)\right)\rangle\rangle\rangle.$$

Since the system is uncorrelated and $\langle\cos(2\phi_l)\rangle = \epsilon$, $\langle\sin(2\phi_l)\rangle = 0$, we immediately obtain

$$\langle\langle Y_2^2 + X_2^2\rangle\rangle = \frac{1}{n} + \frac{n(n-1)\epsilon^2}{n^2}, \tag{C23}$$

in agreement with Eq. (C21).

From Eqs. (C18,C21) we may obtain the expression for the variance of the distribution of the variable-axes moment. A simple formula follows for the case $\epsilon = 0$, where

$$\mathrm{var}(f_2^*) = \frac{1}{n} - \left(\frac{\sqrt{\pi}}{2\sqrt{n}}\right)^2 = \frac{1-\frac{\pi}{4}}{n} \simeq \frac{0.215}{n}. \tag{C24}$$

The scaled variance and scaled standard deviation are

$$\frac{\mathrm{var}(f_2^*)}{f_2^*} \;=\; \frac{\frac{2}{\sqrt{\pi}} - \frac{\sqrt{\pi}}{2}}{\sqrt{n}} \simeq \frac{0.242}{\sqrt{n}},$$
$$\frac{\sigma(f_2^*)}{f_2^*} \;=\; \sqrt{\frac{4}{\pi} - 1} \simeq 0.523. \tag{C25}$$

Note that (for $\epsilon = 0$) there is no dependence on n in the scaled standard deviation. The general case of the dependence of the scaled standard deviation of f_2^* on ϵ for various values of n is shown in Fig. 14. The result is obtained numerically from Eq. (C18,C21).

APPENDIX D: CENTRAL LIMIT THEOREM AND THE MULTIPLE-AXES MOMENTS AND PROFILES

This Appendix contains some details of the application of the central limit theorem to the analysis of the multiple-axes moments and profiles. The calculation is carried out for the case where each harmonic moment has its own rotation angle, as described in Sec. VIII. Define

$$Y_l = \frac{1}{n}\sum_{j=1}^{n} \rho_j^k \cos(l\phi_j), \quad X_l = \frac{1}{n}\sum_{j=1}^{n} \rho_j^k \sin(l\phi_j) \quad \text{(D1)}$$

The rotation angle ϕ^* satisfies

$$\begin{aligned} \cos(l\phi^*) &= Y_l/\sqrt{Y_l^2 + X_l^2}, \\ \sin(l\phi^*) &= X_l/\sqrt{Y_l^2 + X_l^2}, \end{aligned} \quad \text{(D2)}$$

and it depends on the polarity index l. We need the averages

$$\begin{aligned}
\bar{Y}_l &= \int dx_1 \dots dx_n \frac{1}{n}\sum_{j=1}^{\infty} \rho_j^k \cos(l\phi_j) f(x_1, \dots, x_n) = \int d\phi\rho d\rho f(\rho,\phi)\rho^k \cos(l\phi) = I_{k,l}, \quad \text{(D3)} \\
\bar{X}_l &= \int dx_1 \dots dx_n \frac{1}{n}\sum_{j=1}^{\infty} \rho_j^k \sin(l\phi_j) f(x_1, \dots, x_n) = \int d\phi\rho d\rho f(\rho,\phi)\rho^k \sin(l\phi) = 0, \\
\sigma_{Y_l}^2 &= \int dx_1 \dots dx_n \frac{1}{n^2}\sum_{j=1}^{\infty} \rho_j^k \cos(l\phi_j) \sum_{j'=1}^{\infty} \rho_{j'}^k \cos(l\phi_{j'}) f(x_1, \dots, x_n) - (\bar{Y}_l)^2 \\
&= \frac{1}{n}\int d\phi\rho d\rho\rho^{2k} \cos(l\phi)^2 f(\rho,\phi) + \frac{n-1}{n}\left(\int d\phi\rho d\rho\rho^k \cos(l\phi) f(\rho,\phi)\right)^2 - \bar{q}_y^2 \\
&= \frac{1}{2n}\int d\phi\rho d\rho\rho^{2k} f(\rho,\phi)(1+\cos(2l\phi)) - \frac{1}{n}I_{k,l}^2 = \frac{1}{2n}(I_{2k,0} - 2I_{k,l}^2 + I_{2k,2l}) \\
\sigma_{X_l}^2 &= \int dx_1 \dots dx_n \frac{1}{n^2}\sum_{j=1}^{\infty} \rho_j^k \sin(l\phi_j) \sum_{j'=1}^{\infty} \rho_{j'}^k \sin(l\phi_{j'}) f(x_1, \dots, x_n) - (\bar{X}_l)^2 \\
&= \frac{1}{n}\int d\phi\rho d\rho\rho^{2k} \sin(l\phi)^2 f(\rho,\phi) = \frac{1}{2n}(I_{2k,0} - I_{2k,2l}).
\end{aligned}$$

From the central limit theorem, the distribution of Y_l and X_l has the normal form

$$f(Y_l, X_l) = \frac{1}{2\pi\sigma_{Y_l}\sigma_{X_l}} \exp\left[-\frac{(Y_l - \bar{Y}_l)^2}{2\sigma_{Y_l}^2} - \frac{X_l^2}{2\sigma_{X_l}^2}\right]. \quad \text{(D4)}$$

Introducing the q and α variables through

$$Y_l = q\cos\alpha, \quad X_l = q\sin\alpha, \quad \text{(D5)}$$

we can rewrite Eq. (D4) as

$$f(q,\alpha) = \frac{1}{2\pi\sigma_{Y_l}\sigma_{X_l}} \times \exp\left[-\frac{q^2 + \bar{q}_y^2}{2\sigma_{Y_l}^2} + \frac{q\bar{q}_y\cos\alpha}{\sigma_{Y_l}^2} + \delta q^2 \sin^2\alpha\right], \quad \text{(D6)}$$

where

$$\begin{aligned} \delta &= \frac{1}{2\sigma_{Y_l}^2} - \frac{1}{2\sigma_{X_l}^2} \quad \text{(D7)} \\ &= \frac{2n(I_{k,l}^2 - I_{2k,2l})}{(I_{2k,0} - 2I_{k,l}^2 + I_{2k,2l})(I_{2k,0} - I_{2k,2l})}. \end{aligned}$$

Next, we expand in the Taylor series in δ and carry the integration over α, which yields [9, 15]

$$\begin{aligned}
f(q) &= \int_0^{2\pi} d\alpha \exp\left[-\frac{q^2 + (\bar{Y}_l)^2}{2\sigma_{Y_l}^2} + \frac{q\bar{Y}_l\cos\alpha}{\sigma_{Y_l}^2}\right] \times \\
&\sum_{m=0}^{\infty} \frac{(\delta q^2 \sin^2\alpha)^m}{2\pi\sigma_{Y_l}\sigma_{X_l} m!} = \exp\left[-\frac{q^2 + \bar{Y}_l^2}{2\sigma_{Y_l}^2}\right] \sum_{m=0}^{\infty} \left(\frac{2\delta\sigma_{Y_l}^2 q}{\bar{Y}_l}\right)^m \\
&\times \frac{I_m\left(q\bar{Y}_l/\sigma_{Y_l}^2\right)\Gamma\left(m+\frac{1}{2}\right)}{\sqrt{\pi} m! \sigma_{Y_l}\sigma_{X_l}}, \quad \text{(D8)}
\end{aligned}$$

where I_m is the modified Bessel function. The relevant moments of $f(q)$ are

$$\int_0^\infty q\,dq\,f(q) = 1, \tag{D9}$$

$$\int_0^\infty q\,dq\,qf(q) = \frac{\sqrt{2}\sigma^2_{Y_l}}{\sqrt{\pi}\sigma_{X_l}} \sum_{m=0}^{\infty} (2\delta\sigma^2_{Y_l})^m \times \frac{\Gamma\left(m+\frac{1}{2}\right)\Gamma\left(m+\frac{3}{2}\right)\ {}_1F_1\left(-\frac{1}{2}; m+1; -\frac{\bar{Y}_l^2}{2\sigma^2_{Y_l}}\right)}{m!^2},$$

$$\int_0^\infty q\,dq\,q^2 f(q) = \bar{Y}_l^2 + \sigma^2_{Y_l} + \sigma^2_{X_l} = \frac{I_{2k,0} + (n-1)I^2_{k,l}}{n},$$

where ${}_1F_1$ is the confluent hypergeometric function.

From Eq. (D9) one derives immediately the formulas for $l = 2$ listed in the main text as Eq. (7.6,7.8). For a general value of l the result for the variable-axes moments (recall each moment has its own rotation angle) reads

$$\varepsilon^*_{k,l} = \frac{\sqrt{2}\sigma^2_{Y_l}}{I_{k,0}\sqrt{\pi}\sigma_{X_l}} \sum_{m=0}^{\infty} (2\delta\sigma^2_{Y_l})^m \times \frac{\Gamma\left(m+\frac{1}{2}\right)\Gamma\left(m+\frac{3}{2}\right)\ {}_1F_1\left(-\frac{1}{2}; m+1; -\frac{\bar{Y}_l^2}{2\sigma^2_{Y_l}}\right)}{m!^2}, \tag{D10}$$

$$\mathrm{var}(\varepsilon^*_{k,l}) = \frac{I_{2k,0} + (n-1)I^2_{k,l}}{nI^2_{k,0}} - (\varepsilon^*_{k,l})^2.$$

Figure 15 compares the formulas (D10) for the quadrupole case ($l = 2$) with the Monte Carlo simulation in the wounded nucleon model. The difference between the exact Monte Carlo results and the analytic formulas is due to the presence of correlations between the location of sources in Glauber-like models. These correlations result from a rather simple mechanism mentioned at the beginning of Sect. VII: a nucleon from nucleus A may wound several nucleons from nucleus B. This results in some clustering, hence correlations, of the locations of the wounded nucleons. In the derivation of the analytic formulas we have resorted to the central limit theorem, hence all correlations were neglected. The difference between the full and uncorrelated analytic results in Fig. 15 display the significance of the correlations.

The correlations between the locations of sources result in a decrease of the effective number of sources n, so the full result for ε^* (the monotonically rising curves) is naturally above the uncorrelated analytic result. The behavior of the two curves is similar and the relative difference is at the level of 10-15%. For the scaled standard deviation, $\Delta\varepsilon^*/\varepsilon^*$, the comparison is more complicated. At low values of b the two curves are very close, at intermediate b the calculation with correlations is higher, while at peripheric b it is lower than the uncorrelated case. We conclude that at central collisions $\Delta\varepsilon^*/\varepsilon^*$ is not sensitive to correlations.

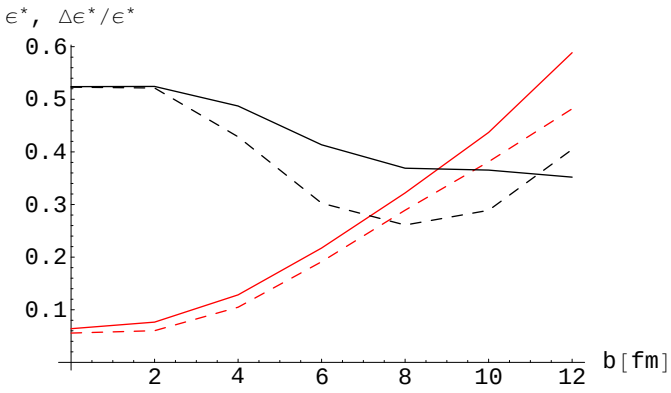


FIG. 15: (Color online) Comparison of the Monte Carlo calculation of $\varepsilon^* = \varepsilon^*_{2,2}$ (the rising curves) and $\Delta\varepsilon^*/\varepsilon^*$ in the wounded nucleon model for gold-gold collisions (solid lines) and the analytic formulas (D10) with $l = 2$ (dashed lines). The analytic formulas neglect correlations between the location of sources present in the full calculation.

In Monte Carlo simulations the correlations may be artificially removed by taking a very large cross section σ_w, in which case all the nucleons get wounded and the correlations between the locations of sources disappear. This may be used for testing purposes. In that case the two calculations of Fig. 15 overlap.

An analytic inclusion of correlations into the framework based on the central limit theorem is difficult and it is more productive to simply perform the simulations. However, the analytic formulas (D10) bare significance not only at the formal level, which helps to understand the nature of the chosen statistical measures. There may be some models where the correlations are largely reduced compared to the wounded nucleon model, or absent. Then the evaluation of ε^* and its variance are simply made by computing the moments $I_{2,0}$, $I_{4,0}$, $I_{2,2}$, and $I_{4,4}$ of the *fixed-axes* distribution and carrying out a truncated series in Eq. (D10). We note that, amusingly, the CGC calculation of $\Delta\varepsilon^*/\varepsilon^*$ shown in Fig. (7) agrees surprisingly well with the uncorrelated result from Fig. (15). This hints that the CGC approach of Ref. [19] has uncorrelated sources.

Next, we derive expressions for the variable-axes profiles $f^*_l(\rho)$ in the absence of particle correlations. These profiles correspond to inclusive distributions unintegrated over the ρ variable of a selected particle, namely

$$2\pi\rho f^*_l(\rho) = \int d\phi \int dx_1 \ldots dx_n f(x_1)\ldots f(x_n) \times \sum_{m=1}^{n} \delta(\rho_m - \rho)\delta(\phi_m - \phi)\cos[l(\phi - \phi^*)], \tag{D11}$$

where the single-particle distributions $f(x_i)$ are normalized to unity. The inclusive distribution is normalized to n, hence $I_{0,0} = \int 2\pi\rho f^*_0(\rho)d\rho = n$. Since all particles have equal distributions $f(x_i)$, we may relabel particles

setting, for instance, $x_n = (\rho, \phi)$ and rewrite Eq. (D11) as

$$f_l^*(\rho) = \int \frac{d\phi}{2\pi} f(\rho,\phi) \int dx_1 \dots dx_{n-1} f(x_1)\dots f(x_{n-1}) \frac{1}{q}\left[\rho^k + \cos(l\phi)\sum_{m=1}^{n-1}\rho_m^k \cos(l\phi_m) + \sin(l\phi)\sum_{m=1}^{n-1}\rho_m^k \sin(l\phi_m)\right], \tag{D12}$$

where we have used the definitions (7.3) and (D5). Similarly to the analysis of the moments of Sect. VII, for sufficiently large values of n the variables

$$Y_l' = \frac{1}{n}\sum_{j=1}^{n-1}\rho_j^k \cos(l\phi_j) = Y_l - \frac{1}{n}\rho^k\cos\phi = q'\cos(\alpha), \quad X_l' = \frac{1}{n}\sum_{j=1}^{n-1}\rho_j^k \sin(l\phi_j) = X_l - \frac{1}{n}\rho^k\sin\phi = q'\sin(\alpha), \tag{D13}$$

follow the normal distribution with rescaled parameters $\bar{Y}_l' = \frac{n-1}{n}\bar{Y}_l$ and $\sigma'^2_{Y_l,X_l} = \frac{n-1}{n}\sigma^2_{Y_l,X_l}$. Therefore

$$\begin{aligned} f_l^*(\rho) &= \int \frac{d\phi}{2\pi} f(\rho,\phi) \int \frac{dq' d\alpha}{2\pi\sigma'_{Y_l}\sigma'_{X_l}} \frac{q'}{q} \exp\left[-\frac{q'^2 + \bar{Y}_l'^2}{2\sigma'^2_y} + \frac{q'\bar{Y}_l\cos\alpha}{\sigma'^2_{Y_l}} + \delta' q'^2 \sin^2\alpha\right]\left[\rho^k + nq'\cos(l\phi-\alpha)\right] \\ &= \int \frac{d\phi}{2\pi} f(\rho,\phi) \int \frac{dq' d\alpha}{2\pi\sigma'_{Y_l}\sigma'_{X_l}} \frac{q'}{\sqrt{q'^2 + 2q'\rho^k\cos(l\phi-\alpha)/n + \rho^{2k}/n^2}} \times \\ &\quad \exp\left[-\frac{q'^2 + \bar{Y}_l^2}{2\sigma'^2_{Y_l}} + \frac{q'\bar{Y}_l\cos\alpha}{\sigma'^2_{Y_l}} + \delta' q'^2\sin^2\alpha\right]\left[\rho^k + nq'\cos(l\phi-\alpha)\right] \end{aligned} \tag{D14}$$

For the case of central collisions, where $\delta' = 0$, $\bar{Y}_l = 0$, and $\sigma'_{Y_l} = \sigma'_{X_l}$, formula (D14) simplifies into

$$\begin{aligned} f_l^*(\rho) &= f_0(\rho)\int \frac{dq' d\beta}{2\pi {\sigma'_{Y_l}}^2} \frac{q'}{\sqrt{q'^2 + 2q'\rho^k/n\cos\beta + \rho^{2k}/n^2}} \exp\left[-\frac{q'^2}{2\sigma'^2_{Y_l}}\right]\left[\rho^k + nq'\cos\beta\right] \\ &= f_0(\rho)\int \frac{dq'}{2\pi {\sigma'_{Y_l}}^2}\exp\left[-\frac{q'^2}{2\sigma'^2_{Y_l}}\right] 2n\left[\left(1+nq/\rho^k\right)E\left(\frac{4nq\rho^k}{\left(\rho^k+nq\right)^2}\right) + \left(1-nq/\rho^k\right)K\left(\frac{4nq\rho^k}{\left(\rho^k+nq\right)^2}\right)\right] \\ &= f_0(\rho)\int \frac{dq'}{2\pi {\sigma'_y}^2}\exp\left[-\frac{q'^2}{2\sigma'^2_y}\right]\pi\rho^k\left(1 + \frac{\rho^{2k}}{8n^2q'^2} + \dots\right), \end{aligned} \tag{D15}$$

where E and K denote the elliptic integrals of the second and third kind. Since q' is of the order of $\sigma'_{Y_l} \sim 1/\sqrt{n}$, subsequent terms in the expansion denoted by $\dots$ are suppressed with powers of n. Hence, in the large-n limit we may retain only the first term in the expansion (the unity). The same result is obtained by first expanding q'/q in inverse powers of n and then carrying the integration over β. The remaining integral over q' is trivial, yielding the final expression for the central case in the absence of correlations:

$$f_l^*(\rho) \simeq \frac{1}{2}\sqrt{\frac{\pi}{nI_{2k,0}}}\,\rho^k f_0(\rho), \qquad (b=0). \tag{D16}$$

Remarkably, in this case all variable-axes profiles are equal to one another and depend only on the monopole profile f_0.

Also note, that the power in the multiplying factor ρ^k simply reflects the (arbitrarily) chosen power for the averaging, thus is a matter of methodology (*cf.* Table I).

We now return to the non-central case of Eq. (D14). We first expand the following piece in the inverse powers, of n, retaining the first two:

$$\begin{aligned} &\frac{(\rho^k + nq'\cos(l\phi-\alpha))q'}{\sqrt{q'^2 + 2q'\rho^k/n\cos(l\phi-\alpha) + \rho^{2k}/n^2}} \\ &= nq'\cos(l\phi-\alpha) + \rho^k\sin^2(l\phi-\alpha) + \dots \end{aligned} \tag{D17}$$

We may then carry the integration over ϕ, which gives

$$f_l^*(\rho) \;=\; \int \frac{dq' d\alpha}{2\pi\sigma'_{Y_l}\sigma'_{X_l}} \exp\left[-\frac{{q'}^2+\bar{Y}_l^{\,2}}{2{\sigma'}^2_{Y_l}} + \frac{q'\bar{Y}_l\cos\alpha}{{\sigma'}^2_{Y_l}} + \delta' {q'}^2\sin^2\alpha\right]\left(nq' f_l(\rho)\cos(\alpha) + \frac{1}{2}\rho^k f_0(\rho) - \frac{1}{2}\rho^k f_{2l}(\rho)\cos(2\alpha)\right) \tag{D18}$$

We note the presence of three fixed-axes profiles: $f_l(\rho)$, $\rho^k f_0(\rho)$, and $\rho^k f_{2l}(\rho)$. The integration over α may be done similarly to the case of the moments, via expansion in the Bessel functions and then carrying out the q' integration. The result, involving various confluent hypergeometric functions, is rather lengthy hence we do not list it here.

[1] C. E. Aguiar, T. Kodama, T. Osada, and Y. Hama, J. Phys. **G27**, 75 (2001), hep-ph/0006239.
[2] C. E. Aguiar, Y. Hama, T. Kodama, and T. Osada, Nucl. Phys. **A698**, 639 (2002), hep-ph/0106266.
[3] M. Miller and R. Snellings (2003), nucl-ex/0312008.
[4] R. S. Bhalerao, J.-P. Blaizot, N. Borghini, and J.-Y. Ollitrault, Phys. Lett. **B627**, 49 (2005), nucl-th/0508009.
[5] R. Andrade, F. Grassi, Y. Hama, T. Kodama, and O. Socolowski, Jr., Phys. Rev. Lett. **97**, 202302 (2006), nucl-th/0608067.
[6] S. A. Voloshin (2006), nucl-th/0606022.
[7] B. Alver et al. (PHOBOS), PoS **CFRNC2006**, 023 (2006), nucl-ex/0608025.
[8] B. Alver et al. (PHOBOS) (2006), nucl-ex/0610037.
[9] P. Sorensen (STAR) (2006), nucl-ex/0612021.
[10] B. Alver et al. (PHOBOS) (2007), nucl-ex/0701049.
[11] A. Białas, M. Błeszyński, and W. Czyż, Nucl. Phys. **B111**, 461 (1976).
[12] B. B. Back et al. (PHOBOS), Phys. Rev. **C65**, 031901 (2002), nucl-ex/0105011.
[13] B. B. Back et al. (PHOBOS), Phys. Rev. **C70**, 021902 (2004), nucl-ex/0405027.
[14] M. Gyulassy, D. H. Rischke, and B. Zhang, Nucl. Phys. **A613**, 397 (1997), nucl-th/9609030.
[15] A. M. Poskanzer and S. A. Voloshin, Phys. Rev. **C58**, 1671 (1998), nucl-ex/9805001.
[16] J.-Y. Ollitrault, Phys. Rev. **D46**, 229 (1992).
[17] T. Hirano, U. W. Heinz, D. Kharzeev, R. Lacey, and Y. Nara, Phys. Lett. **B636**, 299 (2006), nucl-th/0511046.
[18] H. J. Drescher and Y. Nara, Phys. Rev. **C75**, 034905 (2007), nucl-th/0611017.
[19] H.-J. Drescher and Y. Nara (2007), nucl-th/0707.0249.
[20] M. Gyulassy and M. Plumer, Phys. Lett. **B243**, 432 (1990).
[21] R. Baier, Y. L. Dokshitzer, S. Peigne, and D. Schiff, Phys. Lett. **B345**, 277 (1995), hep-ph/9411409.
[22] M. Gyulassy, I. Vitev, and X. N. Wang, Phys. Rev. Lett. **86**, 2537 (2001), nucl-th/0012092.
[23] E. V. Shuryak, Phys. Rev. **C66**, 027902 (2002), nucl-th/0112042.
[24] A. Drees, H. Feng, and J. Jia, Phys. Rev. **C71**, 034909 (2005), nucl-th/0310044.
[25] W. A. Horowitz, Acta Phys. Hung. **A27**, 221 (2006), nucl-th/0511052.
[26] H.-J. Drescher, A. Dumitru, A. Hayashigaki, and Y. Nara, Phys. Rev. **C74**, 044905 (2006), nucl-th/0605012.
[27] S. S. Adler et al. (PHENIX), Phys. Rev. **C69**, 034910 (2004), nucl-ex/0308006.
[28] J.-Y. Ollitrault (1997), nucl-ex/9711003.
[29] N. Borghini, P. M. Dinh, and J.-Y. Ollitrault, Phys. Rev. **C63**, 054906 (2001), nucl-th/0007063.
[30] S. Mrówczyński and E. V. Shuryak, Acta Phys. Polon. **B34**, 4241 (2003), nucl-th/0208052.
[31] S. Vogel, G. Torrieri, and M. Bleicher (2007), nucl-th/0703031.
[32] N. Borghini and J.-Y. Ollitrault, Phys. Lett. **B642**, 227 (2006), nucl-th/0506045.
[33] P. F. Kolb, Phys. Rev. **C68**, 031902 (2003), nucl-th/0306081.
[34] Y. Bai (STAR) (2007), nucl-ex/0701044.